Energy Conversion and Management: X 26 (2025) 101014

Contents lists available at ScienceDirect

Energy Conversion and Management: X

journal homepage: www.sciencedirect.com/journal/energy-conversion-and-management-x

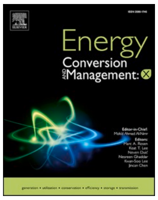

Compatible matching and synergy operation optimization of hydrogen-electric hybrid energy storage system in DC microgrid☆

Banghua Du [a,1], Yanyu Peng [b,1], Yang Li [c], Changjun Xie [a,b,*], Shihao Zhu [b], Wenchao Zhu [d], Yang Yang [a,b], Li You [e], Leiqi Zhang [f], Bo Zhao [f]

[a] *Hubei Key Laboratory of Advanced Technology for Automotive Components, Wuhan University of Technology, Wuhan 430070, China*
[b] *School of Automation, Wuhan University of Technology, Wuhan 430070, China*
[c] *Department of Electrical Engineering, Chalmers University of Technology, Gothenburg 41258, Sweden*
[d] *State Key Laboratory of Advanced Technology for Materials Synthesis and Processing, Wuhan 430070, China*
[e] *State Grid Hubei Electric Power Research Institute, Wuhan 430077, China*
[f] *State Grid Zhejiang Electric Power Research Institute, Hangzhou 310014, China*

ARTICLE INFO

Keywords:
Hydrogen-electric hybrid energy storage
Power allocation
Frequency decomposition
Synergy operation strategy
Synergy operation optimization

ABSTRACT

Hydrogen energy storage (HES) systems could balanced source-load mismatches in DC microgrids. By combining HES with electrical energy storage (EES), the start-up delay and rapid degradation of HES under fluctuating inputs can be mitigated, enhancing system adaptability. However, without proper power allocation and operational optimization, system efficiency and the lifespan of HES and EES decrease. Accordingly, this paper proposes a compatible matching and synergy operation optimization for hydrogen-electric hybrid energy storage systems (H-E HESS). Firstly, Complete Ensemble Empirical Mode Decomposition with Adaptive Noise (CEEMDAN) is developed to decompose power fluctuation signals into frequency components, and the Hilbert transform calculates the energy value to determine high- and low-frequency dividing points. Next, a system power allocation strategy is formulated through the fast response of the EES to compensate for the delay in the start-up of the HES. A multi-objective optimization model is then developed to balance efficiency and lifespan, which is solved by the NSGA-III algorithm. Finally, case studies show that the proposed strategy improves efficiency by 17.95 % and 8.34 %, reduces degradation rates by 1 % and 0.71 %, and shortens system response time in 1 s, compared to Schemes I and II. The strategy's effectiveness is also validated through an experimental platform in a hydrogen-electric coupled DC microgrid demonstration project.

1. Introduction

1.1. Motivation and incitement

Global climate change has accelerated the development of renewable power generation technologies [1]. However, as the penetration of renewable energy continues to increase, its intermittent and fluctuating nature poses significant challenges to modern power systems [2,3]. In addressing these challenges, HES has emerged as a promising solution [4,5]. Nevertheless, HES systems face obstacles such as low conversion efficiency and suboptimal performance under dynamic operating conditions [6,7]. In contrast, electric or EES, exemplified by lithium-ion batteries, excels in rapidly responding to demand fluctuations [8]. Recognizing the complementary characteristics of these storage technologies, H-E HESS have become a novel approach for achieving high-performance and flexible microgrid operations. However, the current lack of mature theoretical methods for developing operational strategies and optimization management for H-E HESS presents a challenge [9]. The mismatch between the supply and demand sides creates bottlenecks in the renewable energy utilization ratio for nearly zero-energy communities. Additional efforts are required to achieve compatibility, coordinated operation, and optimization to ensure efficient collaboration between the HES and EES subsystems.

☆ This article is part of a special issue entitled: 'Hydrogen and Fuel Cells' published in Energy Conversion and Management: X.

* Corresponding author at: Hubei Key Laboratory of Advanced Technology for Automotive Components, Wuhan University of Technology, Wuhan 430070, China.
E-mail address: jackxie@whut.edu.cn (C. Xie).

[1] These authors contributed equally: Banghua Du, Yanyu Peng.

https://doi.org/10.1016/j.ecmx.2025.101014
Received 18 January 2025; Received in revised form 31 March 2025; Accepted 11 April 2025

Nomenclature

Abbreviations

H-E HESS	hydrogen-electric hybrid energy storage system
HES	hydrogen energy storage
EES	electric energy storage
RE	renewable energy
EMS	energy management system
WT	wind turbines
PV	photovoltaic panels
PEMEL	proton exchange membrane electrolyzer
PEMFC	proton exchange membrane fuel cell
HST	hydrogen storage tank
DOD	deep discharge degree
IMF	intrinsic mode function
LC	lifetime cycles

Symbols

P	electricity power, kW
E	energy, kW
Q	quantity of electric energy, MW
V	voltage, V
I	current, A
N	amount of substance, mol
D	voltage degradation values
φ	voltage degradation rate
η	efficiency
n	hydrogen quality, kg
t	time, s/h
v	rate of hydrogen, A/cm^2
a	amplitude
θ	phase
f	frequency
r	residual

Subscripts and Superscripts

HESS,h	high-frequency power
HESS,l	low-frequency power
el	proton exchange membrane electrolyzer
fc	proton exchange membrane fuel cell
sys	system
max	maximum
min	minimum
d	dividing
char	charge
disc	discharge
H_2	Hydrogen

1.2. Literature review

If the hydrogen production process operates at a high frequency, the water electrolysis equipment will run under high load for extended periods, the hydrogen compressor will experience fatigue and wear on its mechanical components due to frequent starting and stopping, shortening its lifetime [10]. The hydrogen storage tank, subjected to frequent charging and discharging, faces severe pressure fluctuations, leading to material fatigue and leakage risks. Fuel cells operating under frequent high loads will see accelerated degradation of their electrode materials, reducing efficiency and lifetime, and potentially leading to safety hazards [11]. Therefore, HES systems need to be combined with fast-response EES systems, such as lithium-ion batteries, to respond to power demand fluctuations quickly. This complementarity not only improves the efficiency and reliability of the energy storage system but also reduces equipment wear and failure risks, thereby extending system lifetime [12]. In recent years, the application of frequency signals as key indicators to optimize the adaptability of various energy storage devices to dynamic power fluctuations has become increasingly widespread. Traditional Fast Fourier Analysis (FFA) is susceptible to power signal instability, resulting in low accuracy for direct signal feature extraction. To achieve multi-scale analysis and improve signal utilization, Hettiarachchi et al. [13] used Empirical Mode Decomposition (EMD) to extract intrinsic mode functions from microgrid net power, smoothing high-frequency fluctuations through supercapacitors to determine the optimal frequency range. Yan et al. [14] and Jiang et al. [15] employed Ensemble Empirical Mode Decomposition (EEMD) to decompose wind and solar energy. Hilbert Transform (HT) is widely used in signal processing to directly obtain the frequency, phase, and amplitude of vibration signals, but it suffers from mode mixing and endpoint effects. Incorporating HT into signal decomposition algorithms endows them with adaptive characteristics, making them better suited for analyzing non-stationary and nonlinear signals. EMD and EEMD face issues of mode mixing and poor stability, prompting the development of CEEMDAN. Feng et al. [16] and Wang et al. [17] highlighted CEEMDAN's superiority in dividing the original signal into stable subsequences. By introducing a step involving HT into the traditional CEEMDAN algorithm, we can more accurately extract the instantaneous frequency and amplitude of signals, enhancing adaptability.

Effectively allocating and managing the power output of each energy source under different operating conditions for the H-E HESS is also crucial for maintaining optimal system performance. Du et al. [18] employed power prediction techniques to alleviate the degradation of electrolyzer and fuel cells, enhancing the system efficiency through heat recovery. Fan et al. [19] proposed an energy management strategy with a fuzzy logic method to foster a net-zero-energy community where both system cost and carbon emissions were reduced. Kamel et al. [20] introduced state machine control strategies with fuzzy logic and frequency decoupling to curtail hydrogen consumption. Han et al. [21] reported a hierarchical energy management approach, dividing the system into local and system control layers to optimize the power distribution between the battery and the fuel cells. Nonetheless, these studies have overlooked the impact of the start-up process of the electrolyzer and fuel cell, leading to wasted and inefficient utilization of power resources and insufficient system response to dynamic power demand.

The control effect of a single strategy relies on engineering experience and cannot guarantee optimal performance metrics. Optimization methods play a major role in maximizing system reliability. The aforementioned HESS optimization decisions typically involve handling a complex multi-objective optimization problem. For instance, Rezk et al. [22] proposed a strategy utilizing the Salp Swarm Algorithm (SSA) and mine blast optimization to manage HESS energy demand response under highly fluctuating load conditions, aiming to minimize fuel consumption and maximize system efficiency. Ferrario et al. [23] identified cost-optimal scaling solutions and improved grid independence through multidimensional sensitivity analysis and Particle Swarm Optimization (PSO) algorithms in four scenarios with different energy management strategies. Li et al. [24] proposed a scheduling method combining Dematel-TOPSIS and Model Predictive Control algorithms to extend system lifetime and reduce costs. Adeyemo et al. [25] optimized annual system costs, potential energy losses, and power losses using the Non-dominated Sorting Genetic Algorithm (NSGA-II). Pu et al. [26] introduced an optimization method based on Random-Triangle Grey Wolf Optimization (RT-GWO) and Mixed Integer Linear Programming to enhance the cost-effectiveness of integrated energy systems. However, during most optimization processes, the degradation of electrolyzers, fuel cells, and EES systems is often overlooked. Ignoring the degradation of storage components during the operation of HESS can lead to inaccurate results in the multi-objective optimization of Loss of Power Supply Probability (LPSP), unmet load, Annualized Cost of System (ACS) [27], Net Present Value (NPV), Net Present Cost (NPC), Levelized Cost of Energy (LCOE), and Loss of Load Probability (LLP). Therefore, it is crucial to model and analyze the operational degradation of hydrogen storage and electric energy storage in the energy management approach.

1.3. Contribution and paper organization

We notice that most of the above papers aim to reduce the overall costs when designing the scheduling or configuration schemes. However, there is a lack of sufficient consideration of the operational characteristics of HESS. The deep integration of HES and EES in the H-E HESS involves three aspects: production, storage, and utilization. Clearly, the system's overall efficiency is affected by the operating characteristics and constraints of the subsystems. The generation has significant fluctuations in renewable energy sources, and the load experiences pronounced temporal variability in multi-dimensional load demands. To enable the coordinated and complementary operation of HES and EES, this paper establishes a model for H-E HESS under microgrid conditions, with which a novel synergy operation strategy considers the frequency of power fluctuation and response time of the system. By reconstructing the system power, high-frequency and low-frequency signals are assigned to EES and HES, respectively. The operating modes and their criteria are classified according to different response speeds, facilitating efficient and reliable system operation. A multi-objective optimization model is developed to improve the energy efficiency and lifetime of the system. The target power parameters in energy management are optimized to achieve the optimal system efficiency and lifetime. Finally, the optimization results are comprehensively compared and analyzed, followed by testing under a demonstration project to validate the feasibility of the proposed synergy operation strategy. The outline of the scheme and the primary contributions of this study are summarized as follows:

1) We established a comprehensive model for H-E HESS operating in microgrid settings to assess the influence of various power allocation and capacity configurations of HES and EES on system performance, including efficiency and degradation.
2) A control strategy for HESS energy management is proposed, improving the CEEMDAN algorithm with an additional Hilbert Transform step based on power fluctuation frequency analysis. It manages power allocation during H-E HESS startup, utilizing electrical energy storage's rapid response to offset energy waste, thereby improving system response speed and ensuring effective power signal decomposition and distribution.
3) To optimize the parameters of the control strategy, a multi-objective optimization model was established under the synergy operation strategy. System lifetime and efficiency were set as performance indicators, and relevant constraints were established. To improve solution accuracy and ensure system performance maximization, the NSGA-III algorithm was used to obtain the Pareto optimal solutions, from which the optimal solution was selected.

2. System description

As shown in Fig. 1, the microgrid under investigation comprises an H-E HESS incorporating HES and EES, renewable energy source (RES) consisting of photovoltaic panels (PV) and wind turbines (WT), and local load. An energy management system (EMS) makes scheduling decisions based on the information of the individual components of the system. The main task of the H-E HESS is to accommodate the imbalanced power between the power generation of the RES and the power consumption of the load. When the RES produces surplus power to meet the load demand, the excessive energy is deposited into the H-E HESS. When the

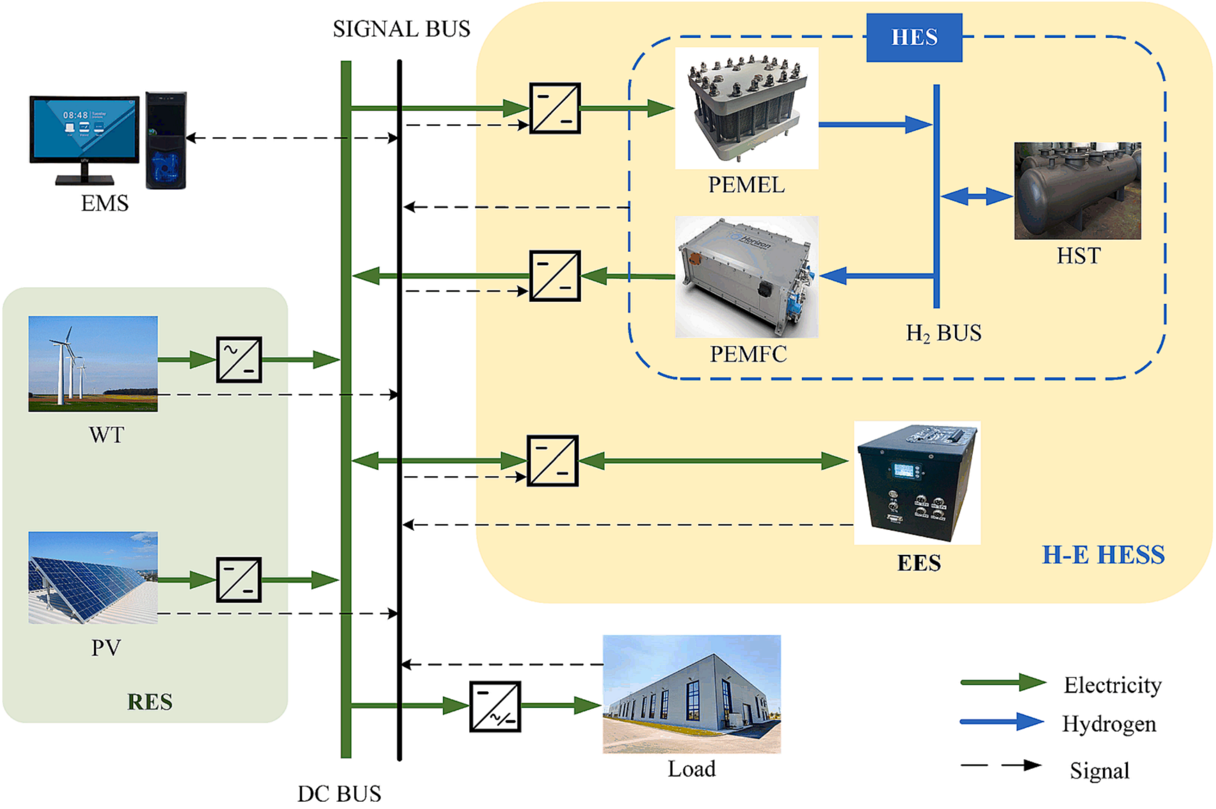

Fig. 1. System configuration of H-E HESS.

RES produces less power than required, the H-E HESS can compensate for the energy deficit, ensuring the continuous and stable operation of the microgrid. The mathematical model of each subsystem in the H-E HESS is developed in this section.

2.1. HES system

The HES system consists of a proton-exchange-membrane electrolyzer (PEMEL), a proton-exchange-membrane fuel cell (PEMFC), and a hydrogen storage tank (HST). The PEMEL absorbs the excess power to produce hydrogen, the HST stores the produced hydrogen, and the PEMFC consumes the hydrogen to generate electricity to compensate for the power deficiency of the system. Since the focus of this paper is mainly on the external behaviors of each component, the detailed multiphysical mechanisms inside the subsystems are not specifically considered. Here, we use a semi-empirical approach to describe the behaviors of the PEMEL and PEMFC stacks.

2.1.1. PEMEL

An empirical current–voltage expression was utilized to establish a static model for the PEMEL system, incorporating the effects of temperature on the overpotentials of the electrodes and the electrolyte [28]. This approach allows for the representation of the current–voltage characteristics as a function of temperature T_{el} variations. PEMEL stack voltage V_{el} at time t can be calculated by:

$$V_{\mathrm{el}}(t) = N_{\mathrm{el}}\left[V_0 + \frac{r_1 + r_1}{A_{\mathrm{el}}} I_{\mathrm{el}}(t) + \left(s_1 + s_2 + s_3 T_{\mathrm{el}}^2\right)\cdot\log\left(\frac{t_1 + t_2/T_{\mathrm{el}} + t_1/T_{\mathrm{el}}^2}{A_{\mathrm{el}}} I_{\mathrm{el}}(t) + 1\right)\right] \tag{1}$$

where N_{el} is the number of single slot series, V_0 is the open circuit voltage of PEMEL, T_{el} is the working temperature of PEMEL, and I_{el} is the PEMEL operating current. r_1 and r_2 are the ohmic resistance parameters of PEMEL, and s_1, s_2, s_3, t_1, t_2, and t_3 are the overvoltage parameters of the PEMEL. In low-temperature electrolysis, the cell voltage will be during normal operation (50–80 °C and 40–300 mA cm^{-2}).

The power of PEMEL P_{el} at time t can be calculated by:

$$P_{\mathrm{el}}(t) = V_{\mathrm{el}}(t) I_{\mathrm{el}}(t) \tag{2}$$

The hydrogen production rate of PEMEL v_{el} at time t can be calculated by:

$$v_{\mathrm{el}}(t) = \eta_{\mathrm{F}} \frac{N_{\mathrm{el}} I_{\mathrm{el}}(t)}{2F} \tag{3}$$

where F is the Faraday's constant and η_{F} is the Faraday's efficiency.

To verify the accuracy of the PEMEL model, this study conducted dynamic performance experiments based on the PEMEL test platform established in the laboratory. Under the conditions of a constant temperature of 353.3 K and a constant pressure of 3 bar for both hydrogen and oxygen, the load current was radually increased from 0 to 3 A/cm^2, and the voltage response was recorded. The goodness of fit between the simulation curve and the experimental data was evaluated according to the root mean square error (RMSE) and the correlation coefficient (R^2) calculated between the experimental voltage and the simulated voltage. The comparison of the polarization curves is shown in the Fig. 2.

As can be seen from Fig. 2, the simulation results of the output voltage model are in good agreement with the experimental data. The output voltage of the stack increases with the increase of the current. When the current undergoes a step − change, the stack temperature will fluctuate to a certain extent. Meanwhile, the intake pressure of the stack also fluctuates, which causes fluctuations in the output voltage curve of the stack. To comprehensively evaluate the performance of the model, this paper uses the root mean square error (RMSE) and the coefficient of determination (R^2) to verify the consistency between the model simulation results and the experimental data.

RMSE is used to measure the average deviation between the model's predicted values and the experimental values. The smaller the RMSE value is, the higher the accuracy of the model will be. The calculation formula is as follows:

$$RMSE = \sqrt{\frac{1}{N}\sum_{i=1}^{N}\left(y_i - \widehat{y}_i\right)^2} \tag{4}$$

where y_i is the i-th experimental measurement value, and $\widehat{y}_i$ is the i-th model prediction value.

R^2 reflects the explanatory ability of the model for the variation of the data. The calculation formula is as follows: The closer the value of R^2 is to 1, the better the goodness of fit of the model will be.

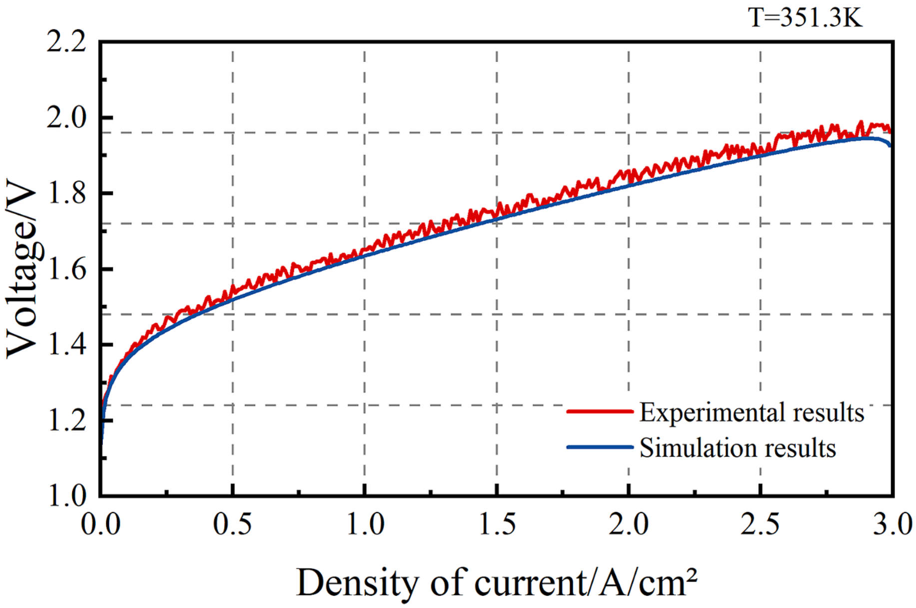

Fig. 2. Comparison of PEMEL output voltage results.

$$R^2 = 1 - \frac{\sum_{i=1}^{N}(y_i - \hat{y}_i)^2}{\sum_{i=1}^{N}(y_i - \bar{y})^2} \tag{5}$$

where $\bar{y}_i$ is the average value of the experimental values.

The RMSE between the model simulation results and the experimental data is 0.032 V, and the R^2 is 0.991, indicating that the model has high accuracy under steady – state operating conditions.

2.1.2. PEMFC

The stack voltage V_{fc} of PEMFC at time t can be calculated by [19]:

$$V_{fc}(t) = N_{fc}\left[V_0 - a_1 \ln(I_{fc}(t)) - a_2 I_{fc}(t) - a_3 e^{a_4 I_{fc}(t)}\right] \tag{6}$$

where $V_0 = 1.23$ V is the open-circuit voltage of the single cell, I_{fc} is the current density of a single cell, and N_{fc} is the number of cells in series. a_1, a_2, a_3, and a_4 are empirical coefficients.

The output power P_{fc} of PEMFC at time t can be calculated by:

$$P_{fc}(t) = V_{fc}(t) I_{fc}(t) \tag{7}$$

The hydrogen consumption rate v_{fc} of PEMFC at time t can be calculated by:

$$v_{fc}(t) = \frac{N_{fc} I_{fc}(t)}{2F\eta_{fc}} \tag{8}$$

where η_{fc} is PEMFC electrical-to-hydrogen conversion efficiency.

To verify the accuracy of the PEMFC (Proton Exchange Membrane Fuel Cell) model, this study carried out dynamic performance experiments based on the PEMFC test platform constructed in the laboratory. Under the conditions of a constant temperature of 353.1 K and a constant pressure of 2 bar for both hydrogen and oxygen, the load current was gradually increased from 0 to 1.5 A/cm^2, and the voltage response was measured. The comparison of the polarization curves is shown in Fig. 3.

As depicted in the provided Fig. 3, the simulation results of the PEMFC output voltage model and the experimental results show a favorable agreement. As the current density increases from 0 to 1.5 A/cm^2, the output voltage of the PEMFC stack exhibits a downward – trending pattern. When the current density experiences a significant change, the internal temperature of the PEMFC stack will vary, and the gas intake pressure will also be affected. These changes lead to fluctuations in the output voltage curve of the stack. By calculating the RMSE and the R^2 between the simulation and experimental data, the RMSE is found to be 0.035 V, and the R^2 is 0.988. This indicates that the PEMFC model has a high degree of accuracy under the given experimental conditions, which validates the reliability of the established PEMFC model in predicting the output voltage characteristics.

2.1.3. HST

The amount of hydrogen n_{HST} stored in the HST at time t can be calculated by:

$$n_{HST}(t) = n_{HST}(t-1) + v_{el}(t-1)\Delta t - v_{fc}(t-1)\Delta t \tag{9}$$

where $t-1$ represents the previous time instance and Δt is the time step.

The level of hydrogen energy (LOH) at time t can be calculated by:

$$\mathrm{LOH}(t) = \mathrm{LOH}(t-1) + n_{HST}(t)/n_{HST,max} \tag{10}$$

where we assume the initial condition is LOH(0) = 0.6 and $n_{HST,max}$ is the maximum amount of hydrogen. The degradation models for HES are included in the objective function of Chapter 4.

2.2. EES system

The behavior of the EES system is described under dynamic charging and discharging conditions. [29] The stored energy in EES at time t can be calculated by [30]:

$$E_{EES}(t) = E_{EES}(t-1) + \left[P_{EES}^{char}(t)\cdot\eta_{EES}^{char} - P_{EES}^{disc}(t)\cdot\eta_{EES}^{disc}\right]\cdot\Delta t \tag{11}$$

where P_{EES}^{char} is charging power, η_{EES}^{char} is charging efficiency, P_{EES}^{disc} is discharging power and η_{EES}^{disc} is discharging efficiency.

The state of charge (SOC) of the EES is

$$\mathrm{SOC}(t) = \mathrm{SOC}(t-1) + \frac{E_{EES}(t)}{Q_{EES}} \tag{12}$$

where we assume the initial condition is SOC(0) = 0.6 and Q_{EES} is the capacity of the EES. The degradation models for EES are included in the objective function of Chapter 4.

3. Synergy operation strategy

The existence of different frequency characteristics and start-up characteristics of HES and EES can negatively affect system efficiency, response time, and service lifetime. To enhance the adaptability of HES

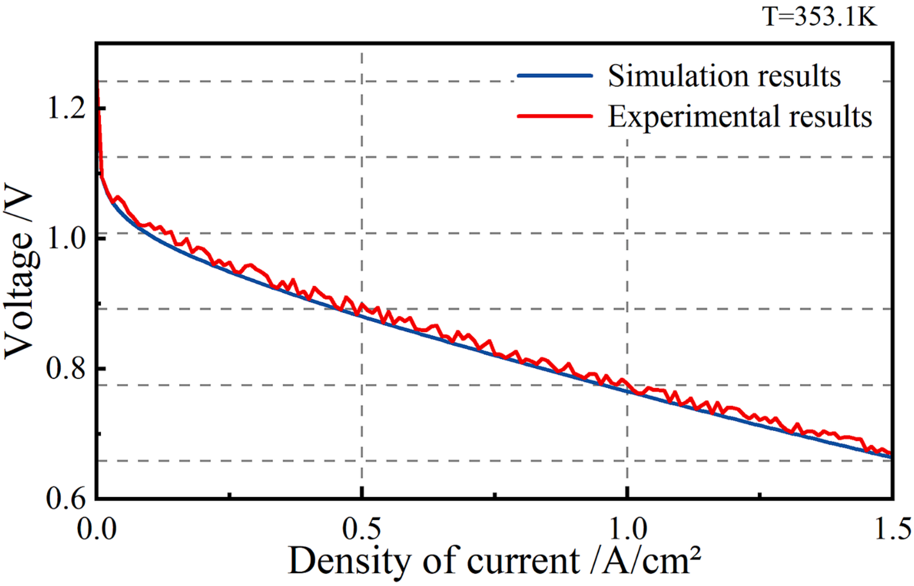

Fig. 3. Comparison of PEMFC output voltage results.

and EES under different scales of power fluctuations at high and low frequencies, a synergy operation strategy is proposed in this section to allocate power. The strategy uses CEEMDAN-HT to decompose the power of the H-E HESS into high-frequency and low-frequency components, which are assigned to the EES and the HES systems, respectively. The start-up characteristics of the subsystems are considered to formulate a specific operation scheme.

3.1. Analysis of frequency characteristics of the power demand

The HES can experience accelerated degradation when it is operated at high-frequency fluctuating power [31,32]. In contrast, EES is more suitable for accommodating these high-frequency power fluctuations. However, a dividing frequency f_d need to be carefully determined to optimally decompose the power signal of the H-E HESS into the high-frequency and low-frequency components.

In the rest of the paper, we denote this power signal as $P_{HESS}(t)$. Considering the non-linear and non-smooth natures of $P_{HESS}(t)$, we can decompose it into a series of intrinsic mode functions (IMFs) with different frequencies and scales [33] based on techniques CEEMDAN. Compared to conventional high-pass filtering and droop control, more effectively captures non-linear and non-stationary characteristics and separates overlapping frequency components. Compared with traditional signal filtering methods, it can better capture the frequency variations of complex non-stationary signals, accurately divide the components, and enhance the adaptability of the system under different power fluctuations [34]. Compared with the method based on optimization, the calculation process of the proposed method is relatively simple, which effectively reduces the complex iterative solution and does not rely on complex optimization model, thus reducing the risk of unreasonable power allocation caused by model error [35]. When compared with learning-based methods, it does not require a large amount of training data and can perform well in scenarios where the data volume is limited. Moreover, the power allocation process is transparent and interpretable, which facilitates system monitoring, maintenance, and optimization adjustments [36].

Additionally, in comparison with EMD and EEMD, CEEMDAN demonstrates lower sensitivity to noise, thus providing more reliable data for system performance analysis. [16]. Nevertheless, since the instantaneous characteristics and frequency information of each IMF is not specifically quantified, it is still not possible to directly determine the optimal dividing frequency f_d from the CEEMDAN results. To solve this problem, in this section, we propose to use the Hilbert transform to quantify the instantaneous characteristics and frequency information of each IMF calculated from CEEMDAN. The specific number of the minimum mixing energy is determined by frequency and amplitude, and the frequency corresponding to the minimum mixing energy is selected as the dividing frequency f_d, which is also the lowest frequency of the modal mixing. We hereinafter denote this improved algorithm as CEEMDAN-HT. Compared with the traditional CEEMDAN, the CEEMDAN-HT proposed in this paper, combining the CEEMDAN with the Hilbert transform, can be more flexible and applicable in dealing with non-linear and non-smooth signals, and effectively avoids modal aliasing in the high-frequency and low-frequency components. The procedure of the selection of the dividing frequency f_d based on CEEMDAN-HT is schematized in Fig. 4 and the flow chart of the algorithm is detailed in Fig. 5.

In the CEEMDAN algorithm, depicted in Fig. 5, the process begins by introducing N sequences of generated Gaussian white noises $n_i(t)$ (where $i = 1, 2, \ldots, N$) to the original signal $P_{HESS}(t)$, resulting in N perturbed signals $P^i_{HESS}(t)$. These perturbed signals $P^i_{HESS}(t)$ are then processed through the Empirical Mode Decomposition (EMD) algorithm to produce N Intrinsic Mode Functions (IMFs), denoted as $IMF_1^N(t)$. The first-order IMF of the CEEMDAN, $IMF_1(t)$, is computed as the average of these N $IMF_1^N(t)$. This procedure is iteratively applied to the residuals to derive higher-order IMFs of the CEEMDAN. This approach effectively addresses the issue of transferring white noise from high-frequency components to low-frequency ones and contributes to minimizing reconstruction errors.

Next, the Hilbert transform is applied to each IMF_k ($k = 1, 2, \ldots, N$) to obtain the corresponding amplitude $a_k(t)$, phase $\theta_k(t)$, and frequency $f_k(t)$. One can use the frequency and amplitude to calculate the mixing energy $E(t)$ between the k-th and $(k-1)$-th IMFs. The frequency corresponding to the minimum $E(t)$ is thus the dividing frequency f_d, which can be used to reconstruct the low-frequency power component $P_{HESS,l}$ and high-frequency power component $P_{HESS,h}$. Introducing the Hilbert transform enables accurate extraction of the frequency, amplitude and phase of each IMF, entailing accurate calculation of the mixing energy for determining the dividing frequency.

To comprehensively evaluate the reconstruction quality following signal decomposition, this study employs four key indicators for quantitative analysis. The effectiveness of the decomposition method is verified across multiple dimensions, using the reconstruction error (RE), Pearson correlation coefficient (PDC), standard deviation error (SDE), and mean absolute percentage error (MAPE). The calculation formulas are as follows:

RE represents the overall deviation for measuring the original signal and the signal reconstructed by CEEMDAN. The smaller the RE value is, the closer the reconstructed signal is to the original signal.

$$RE = \frac{1}{N}\sum_{t=1}^{N}|x_t - \hat{x}_t| \tag{13}$$

Quantify the linear correlation between the original signal and the reconstructed signal. The closer the PDC value is to 1 or −1, the stronger

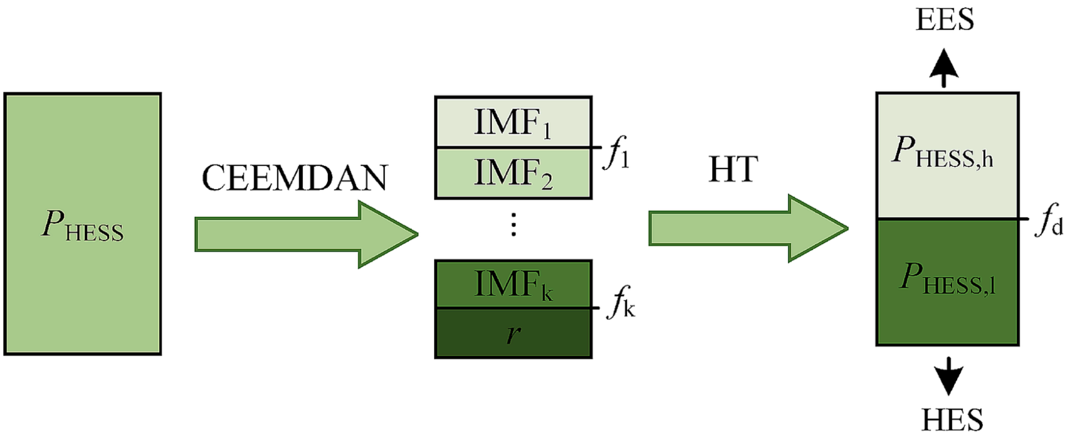

Fig. 4. Schematic diagram of the selection of the frequency dividing points.

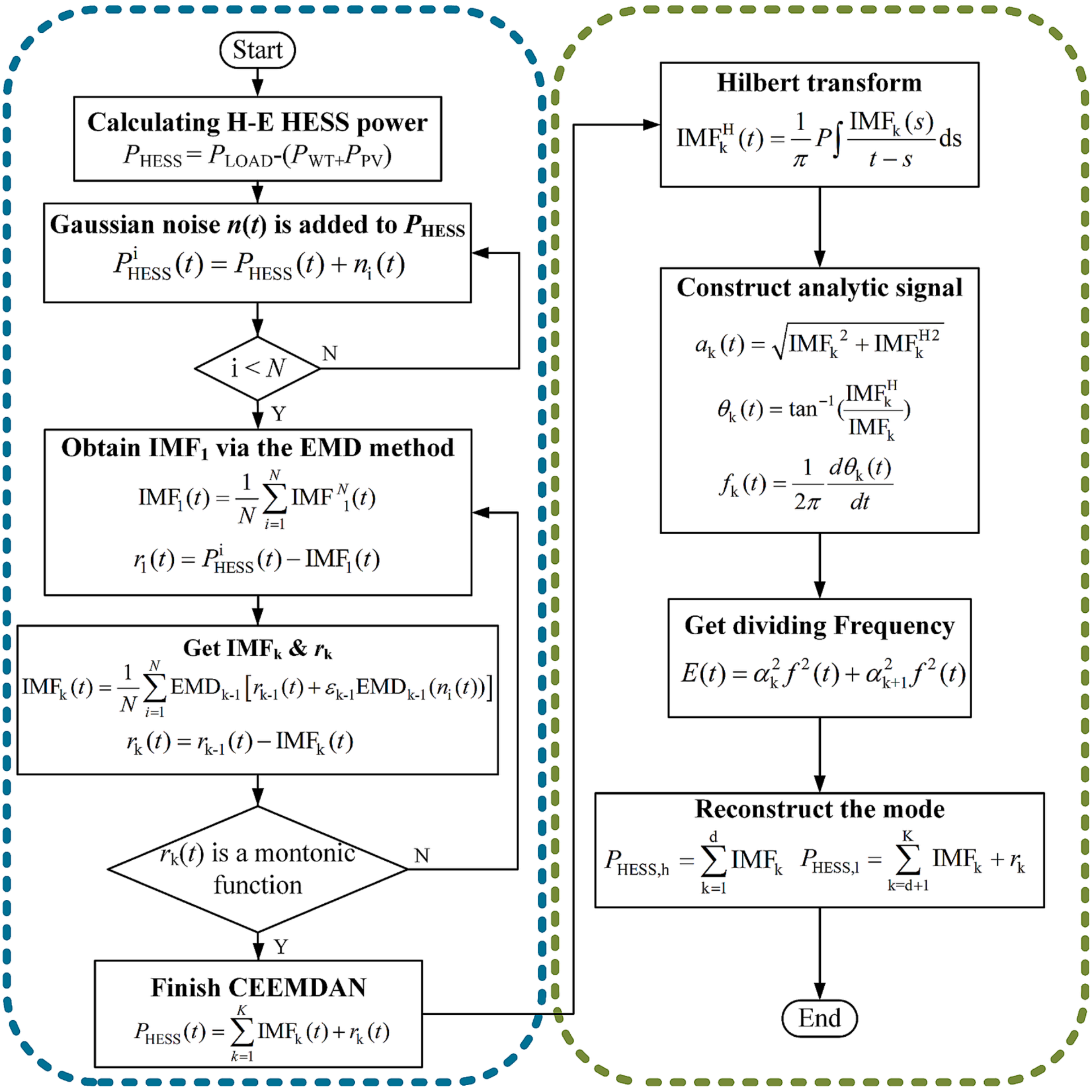

Fig. 5. Flowchart of CEEMDAN-HT reconfiguration of HESS powers.

the correlation is.

$$PDC = \frac{\sum_{i=1}^{N}(x_i - \overline{x})(y_i - \overline{y})}{\sqrt{\sum_{i=1}^{N}(x_i - \overline{x})^2}\sqrt{\sum_{i=1}^{N}(y_i - \overline{y})^2}} \tag{14}$$

Compare the differences in the fluctuation characteristics between the original signal and the reconstructed signal. The smaller the SDE value is, the smaller the error fluctuation will be, and the more stable the prediction or reconstruction result will be.

$$SDE = \sqrt{\frac{1}{N-1}\sum_{t=1}^{N}\left((x_i - \widehat{x}_i) - \frac{1}{N-1}\sum_{t=1}^{N}(x_i - \widehat{x}_i)\right)^2} \tag{15}$$

The mean value of the point-by-point relative errors, which is suitable for the evaluation of non-stationary signals. The smaller the MAPE value is, the smaller the relative error is, and the higher the accuracy will be.

$$MAPE = \frac{1}{N}\sum_{t=1}^{N}\left|\frac{x_i - \widehat{x}_i}{x_i}\right| \tag{16}$$

3.2. Analysis of the start-up characteristics of PEMFC and PEMEL

Once the low-frequency component $P_{\text{HESS,l}}$ is assigned to the HES, the PEMFC enters the start-up phase. PEMFC needs some time for effective transmission of the reactive substances and reaction with the electrodes, ensuring that stable power outputs can be attained. Likewise, the diffusion and reaction between the electrolyte, electrodes and reactive substances at the start-up of PEMEL require a certain period of time and temperature to establish the reaction chain and stabilize the electrolytic process, causing a response delay [37,38]. To better consider these characteristics, start-up tests are performed on an industrial-level PEMEL with a rated power of 220 kW and a PEMFC with a rated power of 200 kW in a hydrogen-electric coupled DC microgrid demonstration project. The start-up of the PEMEL and PEMFC consists of two processes for warm-up and for loading to the rated power. The experimental results and approximate curves of the start-up process are shown in Fig. 6.

From Fig. 6, it can be seen that the whole PEMEL start-up process lasts about 30 min, and it takes about 5 min to load from zero to the rated power. The PEMFC start-up process is about 20 min, and the loading to rated power is 5 min. In contrast, the response time of a typical EES is below 1 s [39], which is negligible in the present study. Therefore, the EES can be utilized to quickly compensate for the power difference between the reference and the actual power in the presence of the delayed response of the HES. This shortens the response time of the system and reduces the waste of energy during the start-up process of hydrogen storage. The EES stops working after the hydrogen storage is completely activated. The start-up waveform schematic is shown in Fig. 7.

Based on the CEEMDAN-HT and the analysis of the start-up characteristics of the energy storage components, a rule-based synergy operation strategy of the H-E HESS is proposed and shown in Fig. 8.

In Fig. 8, the CEEMDAN-HT method is first used to select the dividing frequency f_{d}. Based on f_{d}, the given $P_{\mathrm{HESS}}(t)$ is divided into the high-frequency component $P_{\mathrm{HESS,h}}(t)$ and low-frequency component $P_{\mathrm{HESS,l}}(t)$, which are allocated to the EES and the HES, respectively. The rules in the strategy are described as follows.

When $P_{\mathrm{HESS}} \geq 0$, the H-E HESS is in a discharged state with the following power allocation:

1) The PEMFC powers the low-frequency load. During the PEMFC start-up phase, it slowly releases energy to the DC bus and gradually builds up the power output. After the PEMFC is fully activated, it follows the maximum output power $P_{\mathrm{fc,max}}$ until the LOH reaches the lower limit.
2) The EES supplements the high-frequency power, the energy deficit caused during the start-up phase of the PEMFC, and the difference between the low-frequency system demand $\mathrm{P}^{\mathrm{disc}}_{\mathrm{HESS,l}}$ and the maximum output power of the fuel cell $P_{\mathrm{fc,max}}$ after the full start-up of the PEMFC, until the SOC reaches the lower bound.

When $P_{\mathrm{HESS}} < 0$, the H-E HESS is in the charging mode by following the power allocation rules described below:

1) The PEMEL is responsible for absorbing the excess low-frequency power of the system. During its start-up, the PEMEL power slowly ramps up. Once fully loaded, the PEMEL continues to operate at its maximum power $P_{\mathrm{el,max}}$ until the LOH is saturated.
2) The EES takes the high-frequency power at system frequencies higher than the dividing frequency f_{d}, the power that the PEMEL fails to absorb during its start-up phase, and the discrepancy between the low-frequency power $\mathrm{P}^{\mathrm{char}}_{\mathrm{HESS,l}}$ and the maximum output power $P_{\mathrm{el,max}}$ of PEMEL after it is fully loaded until the SOC reaches its upper limit.

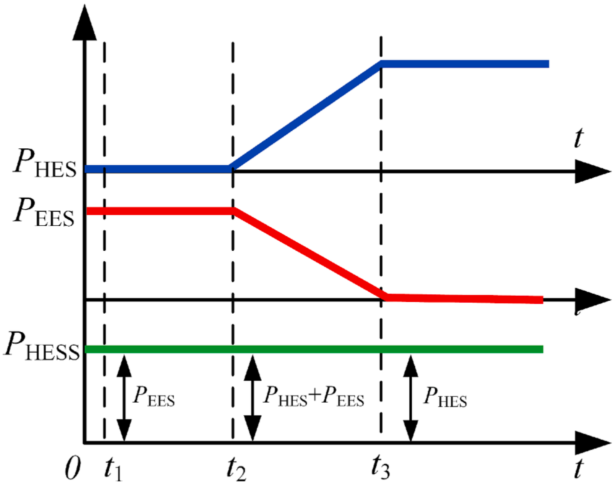

Fig. 7. Schematic diagram of the start-up waveform of H-E HESS.

4. Optimization of design parameters

Since system lifetime and efficiency are significantly affected by the operating power of the HES and EES, we need to consider the influence of the maximum operating power of PEMEL and PEMFC on the operating power of the EES. To optimize the system performance, a multi-objective optimization model under the synergy operation strategy is developed in this section based on two conflicting objective functions, system efficiency and system lifetime. The objective is to determine the power at the actual operating point of the PEMEL and PEMFC to maximize the system efficiency and lifetime.

4.1. Objective functions

1) System efficiency

A high-efficiency system can optimize the utilization of energy resources, minimize energy wastage, and subsequently lower energy costs. Accordingly, an efficiency maximization problem is formulated as described below. To avoid modeling uncertainties introduced by the efficiency-temperature-SOC coupling relationship and reduce parameter sensitivity, and since constant efficiency can effectively decouple the coupling effect between power allocation and loss dynamics during multi-objective operation optimization, constant parameters are chosen in this paper to represent system efficiency [40].

$$\min F_1 = 1 - \eta_{\mathrm{sys}} \tag{17}$$

where

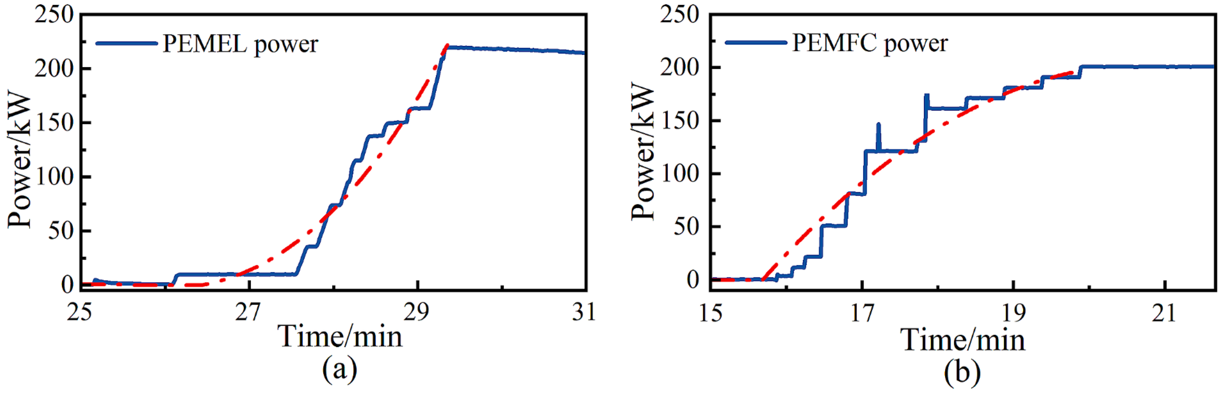

Fig. 6. (a) PEMEL start-up process. (b) PEMFC start-up process.

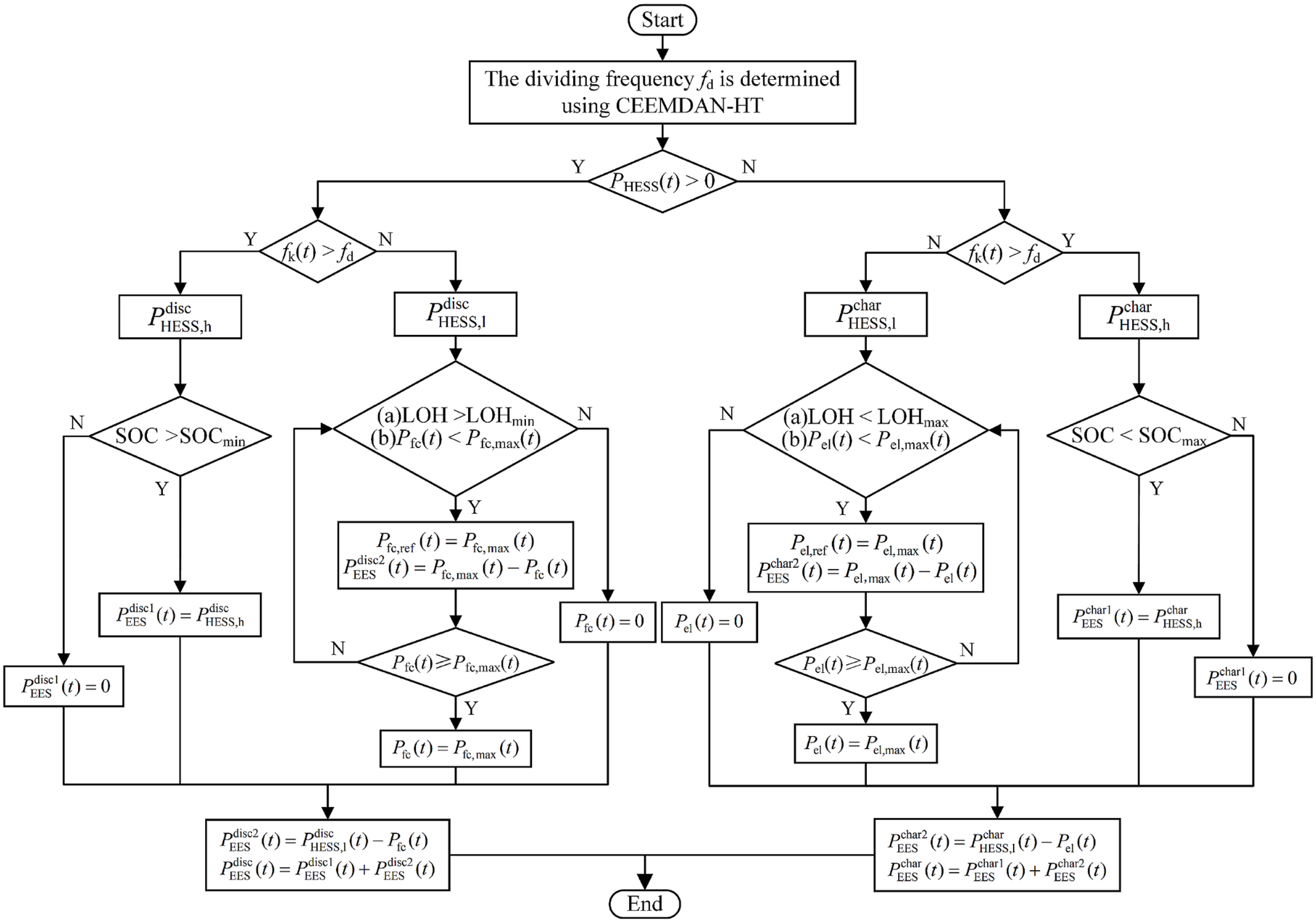

Fig. 8. Flowchart of H-E HESS synergy operation strategy.

$$\eta_{sys} = \begin{cases} (E_{Load} + \Delta E_{H_2} + \Delta E)/E_{RE} & \Delta E_{H_2} \geqslant 0, \Delta E \geqslant 0 \\ (E_{Load} + \Delta E)/(E_{RE} - \Delta E_{H_2}) & \Delta E_{H_2} < 0, \Delta E \geqslant 0 \\ (E_{Load} + \Delta E_{H_2})/(E_{RE} - \Delta E) & \Delta E_{H_2} \geqslant 0, \Delta E < 0 \\ (E_{Load})/(E_{RE} - \Delta E_{H_2} - \Delta E) & \Delta E_{H_2} < 0, \Delta E < 0 \end{cases} \tag{18}$$

and

$$\begin{cases} E_{RE} = (P_{PV}(t) + P_{WT}(t)) \cdot \Delta t \\ E_{Load} = P_{Load}(t) \cdot \Delta t \\ \Delta E_{H_2} = \left(P_{el}(t) \cdot \eta_{el} \cdot \eta_{r,el} - P_{fc}(t) \cdot \eta_{fc} \cdot \eta_{r,fc}\right) \cdot \Delta t \\ \Delta E = \left(P_{EES}^{char}(t) \eta_{EES}^{char} - P_{EES}^{disc}(t) \eta_{EES}^{disc}\right) \cdot \Delta t \end{cases} \tag{19}$$

Here, E_{el} and E_{fc} are the energy absorbed by the PEMEL and the energy generated by the PEMFC, respectively. E_{Load} and E_{RE} are consumed energy by the load and energy generated by the RES, respectively. ΔE and ΔE_{H2} are the energy changes in the EES and HES over 168 h, respectively. The efficiencies of the interface converters associated with the PEMEL, denoted as $\eta_{r,el}$, and those of the PEMFC, denoted as $\eta_{r,fc}$, are considered to be constant.

2) System lifetime

The lifetime of the energy storage devices can be used to assess the reliability and durability of the H-E HESS, which is beneficial for enhancing operational planning and energy management practices. The longevity of the system is evaluated through the performance degradation rate of each energy storage device. A lower performance degradation rate signifies an extended system lifetime. This is given as

$$\begin{aligned} \min F_2 = \varphi_{HESS} &= c_1\varphi_{el} + c_2\varphi_{fc} + c_3\varphi_{EES} \\ &= c_1\frac{D_{el}}{10\% V_{e,el}} + c_2\frac{D_{fc}}{10\% V_{e,fc}} + c_3\sum_{i=1}^{9}\left(\frac{D_{EES,i}}{LC_{b,i}}\right) \end{aligned} \tag{20}$$

where φ_{HESS} is the performance degradation rate of the H-E HESS. φ_{el}, φ_{fc}, and φ_{EES} are the performance degradation rates of PEMEL, PEMFC, and EES, respectively. c_1, c_2, and c_3 are corresponding weighting factors, and they are selected as 1 to reflect the equal significance of the three devices. Furthermore, D_{el} and $V_{e,el}$ represent the voltage degradation and the rated voltage of the PEMEL, respectively. D_{fc} and $V_{e,fc}$ represent the voltage degradation and the rated voltage of the PEMFC, respectively. For the EES, the degradation is evaluated according to the depth of discharge (DOD). Specifically, we consider nine DOD intervals, denoted by DOD$_i$ (i = 1, 2, …, 9) and their SOC ranges are defined in

Table 1
DOD intervals and life cycles.

DOD$_i$	DOD interval	LC$_{b,i}$
DOD$_1$ (10 %)	5–15 %	70,000
DOD$_2$ (20 %)	15–25 %	31,000
DOD$_3$ (30 %)	25–35 %	18,100
DOD$_4$ (40 %)	35–45 %	11,800
DOD$_5$ (50 %)	45–55 %	8100
DOD$_6$ (60 %)	55–65 %	5800
DOD$_7$ (70 %)	65–75 %	4300
DOD$_8$ (80 %)	75–85 %	3300
DOD$_9$ (90 %)	85–100 %	2500

Table 1. For each DOD interval, $D_{\mathrm{EES},i}$ is the capacity loss and $LC_{\mathrm{b},i}$ is the maximum number of charge/discharge cycles allowed. The values of all $LC_{\mathrm{b},i}$ are also provided in Table 1.

The degradation parameters D_{el}, D_{fc}, and D_{EESi} can be calculated as

$$\begin{cases} D_{\mathrm{el}} = D_{ss,\mathrm{el}} + D_{fh,\mathrm{el}} + D_{fl,\mathrm{el}} = k_{ss,\mathrm{el}}\cdot n_{ss,\mathrm{el}} + k_{fh,\mathrm{el}}\cdot t_{fh,\mathrm{el}} + k_{fl,\mathrm{el}}\cdot t_{fl,\mathrm{el}} \\ D_{\mathrm{fc}} = D_{ss,\mathrm{fc}} + D_{id,\mathrm{fc}} + D_{lc,\mathrm{fc}} + D_{hc,\mathrm{fc}} = k_{ss,\mathrm{fc}}\cdot n_{ss,\mathrm{fc}} + k_{id,\mathrm{fc}}\cdot t_{id,\mathrm{fc}} + k_{lc,\mathrm{fc}}\cdot t_{lc,\mathrm{fc}} + k_{hc,\mathrm{fc}}\cdot t_{hc,\mathrm{fc}} \\ D_{\mathrm{EES},i} = N_{\mathrm{bc},i}\cdot N_{\mathrm{day}} \end{cases} \tag{21}$$

where $D_{ss,\mathrm{el}}$, $D_{fh,\mathrm{el}}$, and $D_{fl,\mathrm{el}}$ are the voltage degradations of PEMEL caused by its start-stop, high power fluctuations, and low power fluctuations, respectively [41]. $k_{ss,\mathrm{el}}$ is the degradation coefficient for the PEMEL start-stops, $n_{ss,\mathrm{el}}$ is the average number of PEMEL start-stop cycles, and $k_{fl,\mathrm{el}}$ and $t_{fl,\mathrm{el}}$ are the PEMEL degradation coefficient and the average operation time for PEMEL high-power fluctuations, respectively. $D_{ss,\mathrm{fc}}$, $D_{lc,\mathrm{fc}}$, $D_{hc,\mathrm{fc}}$, and $D_{id,\mathrm{fc}}$ represent the voltage degradations of PEMFC caused by start-stops, low load operations, high load operations, and loading variations, respectively [42]. $k_{ss,\mathrm{fc}}$ is the degradation coefficient for the PEMFC start-stops, and $n_{ss,\mathrm{fc}}$ is its average start-stop cycle number. $k_{lc,\mathrm{fc}}$ and $t_{lc,\mathrm{fc}}$ are the degradation coefficient and the average operation time of PEMFC low power fluctuations, respectively. $k_{hc,\mathrm{fc}}$ and $n_{hc,\mathrm{fc}}$ are the degradation coefficient and the average operation time of PEMFC high power fluctuations, respectively. $k_{id,\mathrm{fc}}$ and $t_{id,\mathrm{fc}}$ denote the degradation coefficient and the average magnitude of PEMFC power variations, respectively [43]. Furthermore, $D_{\mathrm{EES},i}$ is obtained as the product of the total operation days N_{day} and a parameter $N_{\mathrm{bc},i}$, where $N_{\mathrm{bc},i}$ is calculated by the rainflow counting method [31,44]. The values of these parameters used in this paper are given in Table 2.

4.2. Constraints

The operation of the system is constrained by power balance, capacity, power limits, and lifetime of the different devices. These constraints are presented in this subsection.

1) Power balance

The following power balance constraint is imposed to ensure the energy supply meets the demand at all times:

$$P_{\mathrm{el}}(t) + P_{\mathrm{Load}}(t) + P_{\mathrm{EES}}^{\mathrm{char}}(t) = P_{\mathrm{WT}}(t) + P_{\mathrm{PV}}(t) + P_{\mathrm{EES}}^{\mathrm{disc}}(t) + P_{\mathrm{fc}}(t) \tag{22}$$

2) HES constraints

HST capacity constraint:

$$\mathrm{LOH}_{\mathrm{min}} \leqslant \mathrm{LOH} \leqslant \mathrm{LOH}_{\mathrm{max}} \tag{23}$$

PEMEL and PEMFC operating power constraints:

$$\begin{cases} 0.1P\mathrm{el},\mathrm{N} \leqslant P_{\mathrm{el}}(t) \leqslant P_{\mathrm{el,max}}(t) \leqslant P_{\mathrm{HESS,1}}^{\mathrm{char}}(t) \\ 0.1P\mathrm{fc},\mathrm{N} \leqslant P_{\mathrm{fc}}(t) \leqslant P_{\mathrm{fc,max}}(t) \leqslant P_{\mathrm{HESS,1}}^{\mathrm{disc}}(t) \end{cases} \tag{24}$$

Table 2
HES and EES parameters.

Parameters	Value	Parameters	Value
$k_{ss,\mathrm{el}}$	30 μV/cycles	$k_{ss,\mathrm{fc}}$	23.91 μV/ cycles
$k_{fh,\mathrm{el}}$	50 μV/h	$k_{lc,\mathrm{fc}}$	10.17 μV/h
$k_{fl,\mathrm{el}}$	66 μV/h	$k_{hc,\mathrm{fc}}$	11.74 μV/h
η_{el}	0.6	$k_{id,\mathrm{fc}}$	0.123 μV/kW
$\mathrm{LOH}_{\mathrm{max}}/\mathrm{LOH}_{\mathrm{min}}$	0.9/0.1	η_{fc}	0.7
$\mathrm{SOC}_{\mathrm{max}}/\mathrm{SOC}_{\mathrm{min}}$	0.8/0.2	$\eta_{\mathrm{EES}}^{\mathrm{char}}$	0.945
$\eta_{\mathrm{r,el}}$	0.95	$\eta_{\mathrm{EES}}^{\mathrm{disc}}$	0.9
$\eta_{\mathrm{r,fc}}$	0.95	–	–

PEMEL and PEMFC lifetime constraints:

$$\begin{cases} 0 \leqslant \varphi_{\mathrm{el}} \leqslant 1 \\ 0 \leqslant \varphi_{\mathrm{fc}} \leqslant 1 \end{cases} \tag{25}$$

3) EES constraints

EES capacity constraint:

$$\mathrm{SOC}_{\mathrm{min}} \leqslant \mathrm{SOC} \leqslant \mathrm{SOC}_{\mathrm{max}} \tag{26}$$

EES lifetime constraint:

$$0 \leqslant \varphi_{\mathrm{EES}} \leqslant 1 \tag{27}$$

4.3. Optimization algorithm

As mentioned in Section 4.1, the optimization objective is to improve system efficiency and extend system lifetime, which creates a multi-objective optimization problem. Achieving efficiency can conflict with extending lifetime, resulting in significant complexity and scale. The solutions form a non-dominated relationship known as the Pareto solution set. While metaheuristic methods such as the ant colony algorithm and particle swarm optimization can address multi-objective problems [45], they often face challenges like local optimization or high computational demands for accurate solutions.

In contrast, in this work, the NSGA-III algorithm can be used to solve the presented multi-objective optimization problem, and the specific optimization process is shown in Fig. 9. NSGA-III leverages the diversity of reference points to maintain the speed and effectiveness of the search process. The core mechanism of NSGA-III focuses on maintaining diversity within the population. The algorithm can be adapted to multi-objective scenarios by employing an improved selection mechanism, preventing convergence to a single region of the solution space [46]. This emphasis on Pareto front diversity ensures a comprehensive exploration of trade-offs, which is beneficial not only for multi-objective but also for bi-objective optimization problems [47], so it is considered a preferable choice for bi-objective optimization problems with complex operational constraints [48]. Its iterative process can generate rich Pareto frontiers, providing decision-makers with a broader range of options [49,50].

Step 1: Input RES and load data, define decision variables ($P_{\mathrm{el,max}}$ and $P_{\mathrm{fc,max}}$) and decision variable constraints, system energy flow constraints, and lifetime constraints. Randomly initialize the parent population $P_1 = [P_{\mathrm{el,max}}, P_{\mathrm{fc,max}}]$ with a population size of M in the allowed decision variable search space.

Step 2: The objective functions F_1 and F_2 corresponding to each individual are calculated by substituting the size of M parent population P_1 into the synergy operation strategy, and the objective function values F_1 and F_2 of each individual in the parent population P_1 are subjected to the preservation of the elite generation (crossover, mutation, and selection), and nondominated sorting operations, to obtain an offspring population R_1 with a size of N.

Step 3: A population Q_n of size 2 N is obtained by mixing the

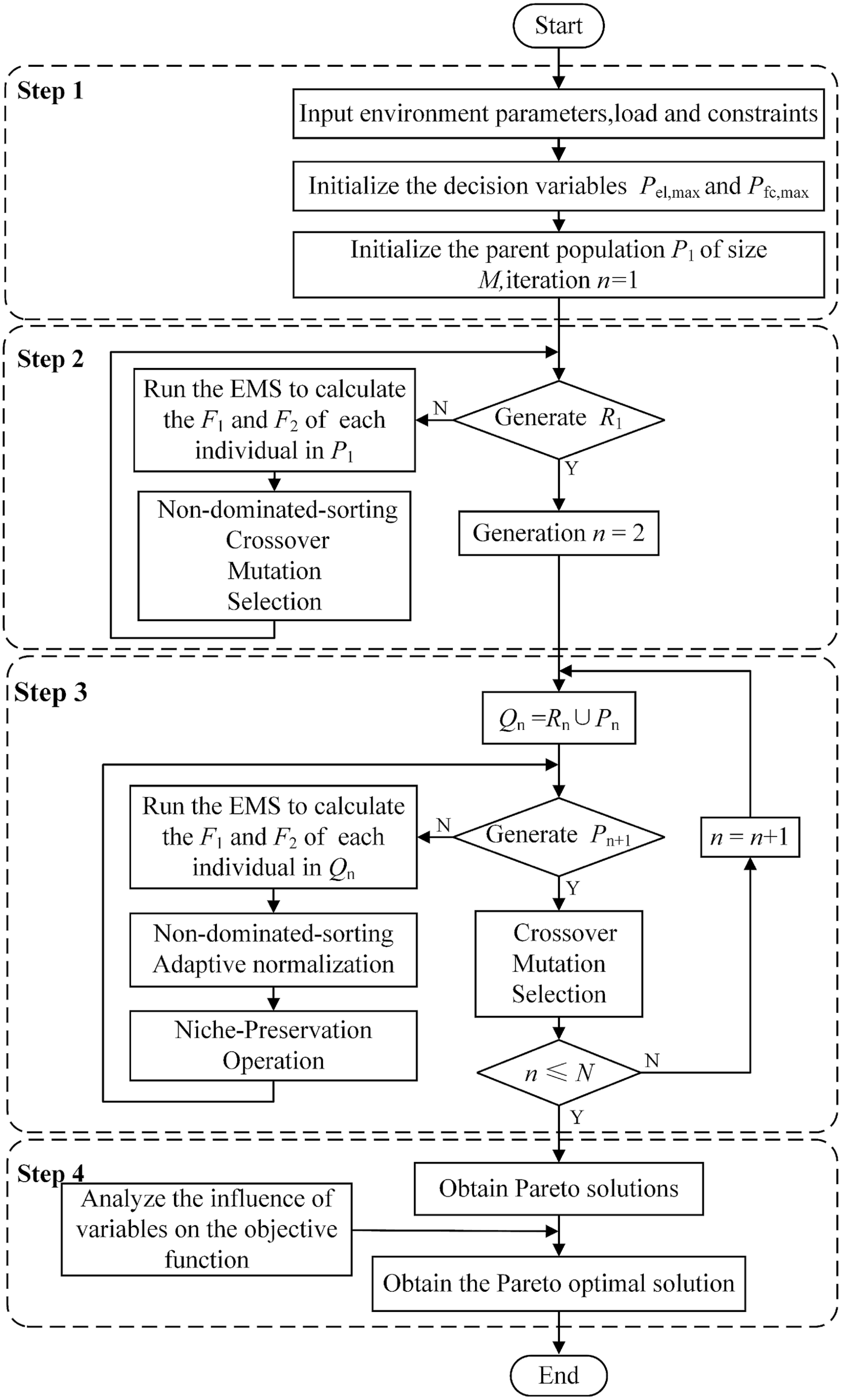

Fig. 9. Flowchart of NSGA-III algorithm operation.

populations P_n and R_n. The size of the 2 N parent population Q_n is substituted into the synergy operation strategy to calculate the corresponding objective functions F_1 and F_2 for each individual, and the objective function values F_1 and F_2 for each individual of Q_n are quickly non-dominated sorted. The individuals in the top half of the non-dominated sort are selected to create a new population. Next, a niche and a normalized mechanism are executed on the population, where each individual is associated with a specific reference point based on the shortest vertical distance of each individual in the population. Dynamic niche methods or crowding distance adjustments. This helps ensure a varied population, reducing the risk of premature convergence The final niche mechanism selects the individual associated with the smallest reference point in P_{n+1} to go into the next generation until the maximum number of iterations is reached.

Step 4: The Pareto frontier solution is obtained. The variation of decision variables in the synergy operation strategy is analyzed in terms of its influence on the objective function, and the Pareto optimal solution is selected among the Pareto frontier solutions that take into account the system efficiency and lifetime.

5. Case study

5.1. System configuration

A H-E-HESS coupled DC microgrid demonstration project located in the coastal area of China is selected to verify the proposed cooperative operation strategy, and the composition of this demonstration project is shown in Fig. 10. The model parameters regarding the system specifications were obtained and given in Table 3. The 168-hour RES and load data for this study are obtained from four typical scenarios at different wind and solar fluctuation levels. Typical data of the four scenarios are shown in Fig. 11.

Table 3
System specifications.

Parameter	Value	Parameter	Value
P_{PV} /kW	500	$V_{e,fc}$ /V	540
P_{WT} /kW	200	$P_{fc,N}$ /kW	200
$V_{e,el}$ /V	200	Q_{EES}/MWh	1.54
$P_{el,N}$ /kW	220	$n_{hst,max}$ /kg	400

In Fig. 11, the four scenarios exhibit a stratified phenomenon based on the net difference between source and load. Moreover, the wind and solar fluctuations vary significantly across different scenarios. Among these scenarios, TS1 and TS2 have abundant wind and solar resources with significant fluctuations, while TS3 and TS4 feature relatively scarce wind and solar resources, resulting in smaller fluctuations. In this study, the effectiveness of the proposed synergy operation strategy is verified through these four scenarios, each characterized by varying levels of RES availability. For devices such as PEMEL and PEMFC, their performance will change gradually during continuous operation. The 168-hour time window effectively captures the typical weekly cycle of power system loads, accounting for the variations between 5 working days and 2 rest days. Historical data analysis indicates that this duration can cover the vast majority of extreme low-output events in renewable generation. By analyzing system behavior over 168 h, the optimal coordination among subsystems in the hydrogen-electricity DC microgrid can be determined, enabling a comprehensive evaluation of performance impacts on overall operation. Therefore, this study adopts a 168-hour time scale for scenario analysis.

5.2. Power distribution analysis of H-E HESS

The objective of this study is to develop an optimal synergy operation strategy for an H-E HESS under consideration of lifetime and response

Fig. 10. Hydrogen-electric coupled DC microgrid demonstration project.

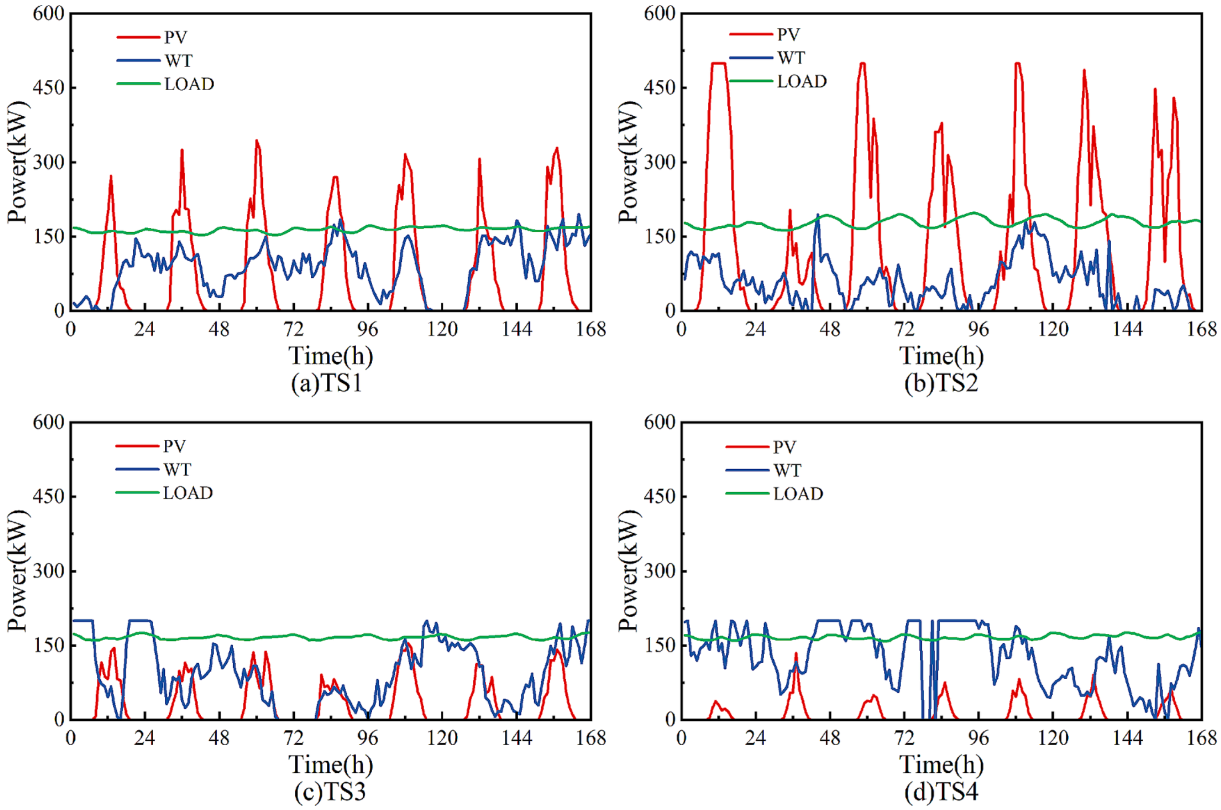

(a)TS1 (b)TS2 (c)TS3 (d)TS4

Fig. 11. RES and load data under four typical scenarios.

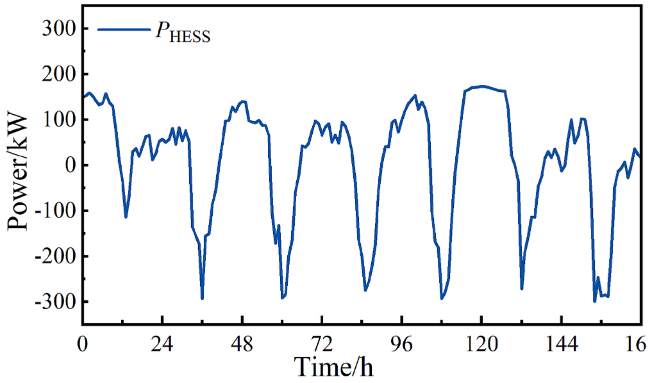

Fig. 12. Schematic diagram of H-E HESS power fluctuation for TS1.

time. For demonstrative purposes, the power P_{HESS} of the H-E HESS of TS1 is selected and shown in Fig. 12.

The method analyzes the collected data in MATLAB 2021b and is solved on an Intel(R) Core(TM) i5-12500H CPU @ 2.50 GHz and 16.00 GB RAM workstation to decompress the nonlinear HESS power fluctuation frequency signal into simpler IMFs. In the CEEMDAN process, the noise standard deviation((Nstd), realizations (NR), and maximum iterations of 5000 (MaxIter) were set to 0.2, 20, and 500, respectively. By CEEMDAN, P_{HESS} is decomposed into the seven IMFs and a residual component, as shown in Fig. 13.

From Fig. 13, it can be observed that there are significant differences in the magnitude and frequency of different IMFs. To clearly reflect the more accurate extraction of the instantaneous frequency and amplitude of each IMF and enhance the adaptability of the algorithm, an HT transform is applied. This transform converts the original signal from an amplitude-time–frequency triplet to an amplitude-frequency relationship. The results are shown in Fig. 14.

From Fig. 14, it can be seen that due to the complex composition of the original signal, mode aliasing cannot be completely avoided by using the CEEMDAN, reflected by the non-zero overlapping areas. However, it is also observed that the overlapping area between IMF4 and IMF5 and the corresponding energy of the mixed signals $E(t)$ is 0.139, the lowest among all cases. This fact indicates that IMF4 and IMF5 are characterized by the lowest level of mode aliasing, where the high- and low-frequency dividing frequency f_{d} can be readily selected as 1.81×10^{-5} Hz, as shown in Fig. 14. Hence, IMF_1-IMF_4 are reconstructed to obtain the high-frequency component $P_{\text{HESS,h}}$, assigned to the EES, while the rest components, i.e., IMF_5- IMF_5 as well as r, are reconstructed as the low-frequency power $P_{\text{HESS,h}}$ assigned to the HES.

In addition, in order to more intuitively analyze the advantages of CEEMDAN-HT for the hydrogen-electric hybrid energy storage system constructed in this paper based on data, the results of the EMD-HT method, EEMD-HT method, and CEEMDAN-HT method are analyzed and compared. The reconstruction errors of the power sequences of a certain system decomposed by the three algorithms, namely EMD, EEMD, and CEEMDAN, are shown in Fig. 15.

From Fig. 15, Through experimental analysis, during EEMD signal reconstruction, residual white noise causes a large error:0.0118. EEMD's noise – introduction, especially for low – frequency signals, disturbs the result and reduces accuracy. In contrast, CEEMDAN's reconstruction error is near 8.2334×10^{-17}, similar to EMD, showing its advantage. By adding paired white noises in decomposition, CEEMDAN eliminates residual noise, reducing errors and ensuring signal integrity. This mechanism helps CEEMDAN remove noise interference without losing key information, guaranteeing modal component accuracy and better reflecting signal local features. Other reconstruction error index results are in Table 4.

Through the comparative analysis of the three frequency division methods, namely EEMD, EMD, and CEEMDAN, in Table 4, CEEMDAN shows significant advantages in signal decomposition and reconstruction. Its reconstruction error(RE) is extremely low, with a value of

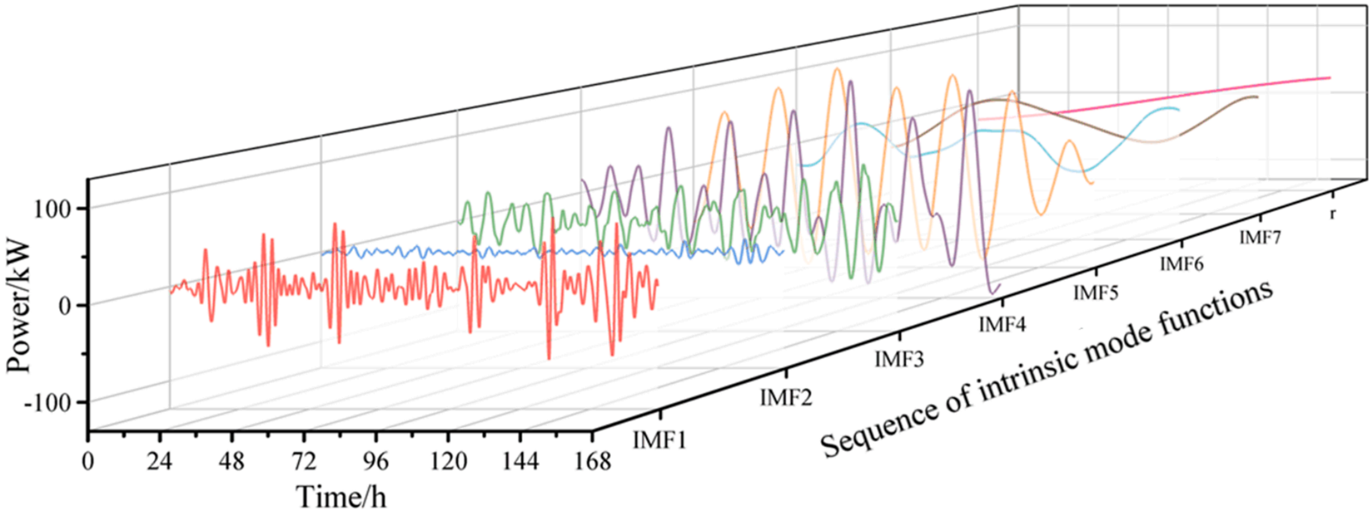

Fig. 13. Power signal decomposition results based on CEEMDAN for TS1.

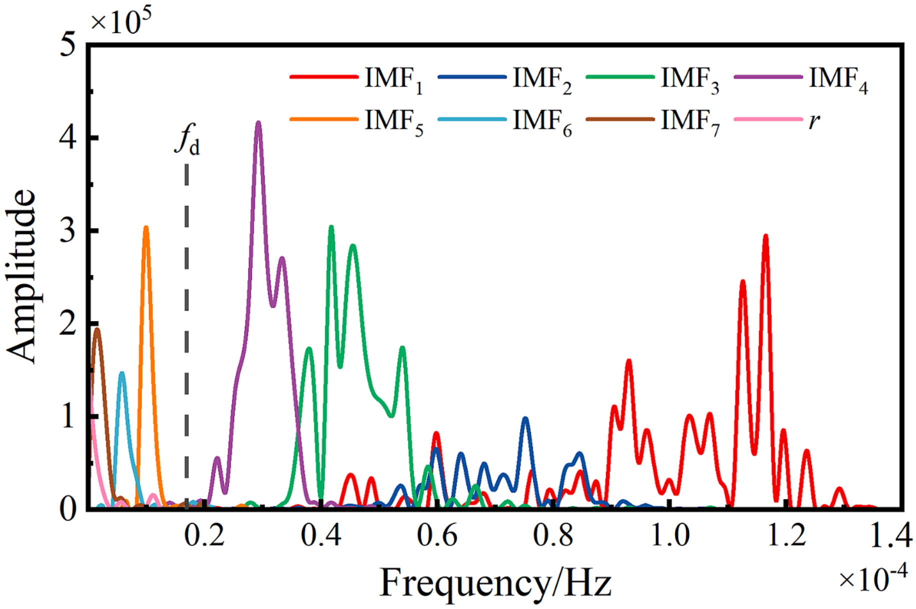

Fig. 14. Marginal spectrum obtained by CEEMDAN-HT for TS1.

8.2334×10^{-17}, and the Pearson correlation coefficient(PCC) is 1, indicating that it can completely maintain the correlation of the original signal. At the same time, the standard deviation error(SDE) of 1.4750×10^{-14} and the mean absolute percentage error(MAPE) of 1.2966×10^{-14} are almost negligible. Compared with EEMD, CEEMDAN is more outstanding in terms of accuracy and stability, and its performance is equivalent to or even better than that of EMD, especially showing stronger adaptability and reliability when dealing with complex signals. The result is shown in Fig. 16.

As can be seen in Fig. 16, compared to the original power signal P_{HESS}, after the high-frequency and low-frequency allocation by CEEMDAN-HT, $P_{\mathrm{HESS,l}}$ is allocated to HES and $P_{\mathrm{HESS,h}}$ to EES. The maximum power fluctuation amplitude of HES decreased by 216.35 kW, and the peak power decreased by 199.59 kW.

The power of PEMEL and the charging power of EES are shown in Fig. 17(a). The EES quickly responds to the difference between the target power and the actual power of PEMEL during the start-up process of the PEMEL. After the start-up process, the PEMEL becomes the sole device to handle the low-frequency power. On the other side, the PEMFC power and the discharging power of EES are shown in Fig. 17(b). The EES can discharge rapidly to compensate for the lack of power during the processes of PEMFC start-up until the PEMFC output power can follow the low-frequency load power.

5.3. Optimization results

Based on the NSGA-III optimization algorithm described in Section 4.3, the effect of variation of decision variables $P_{\mathrm{el,max}}$ and $P_{\mathrm{fc,max}}$ on the system efficiency can be explored. The population size and the number of iterations are set to 300 and 100 to ensure the reliability of the optimization results. The results are illustrated in Fig. 18.

Fig. 18(a) shows a 3D map that describes the relationship between $P_{\mathrm{el,max}}$, $P_{\mathrm{fc,max}}$, and system efficiency. For better visualization, the surface of Fig. 18(a) is projected in Fig. 18(b) as the contour in the $P_{\mathrm{el,max}} - P_{\mathrm{fc,max}}$ plane. It can be seen that the system efficiency is approximately proportional to $P_{\mathrm{el,max}}$ and inversely proportional to $P_{\mathrm{fc,max}}$. Furthermore, a higher system efficiency can be gained when $P_{\mathrm{el,max}} \geq 110$ kW, in which condition the corresponding $P_{\mathrm{fc,max}}$ is between 80 kW and 100

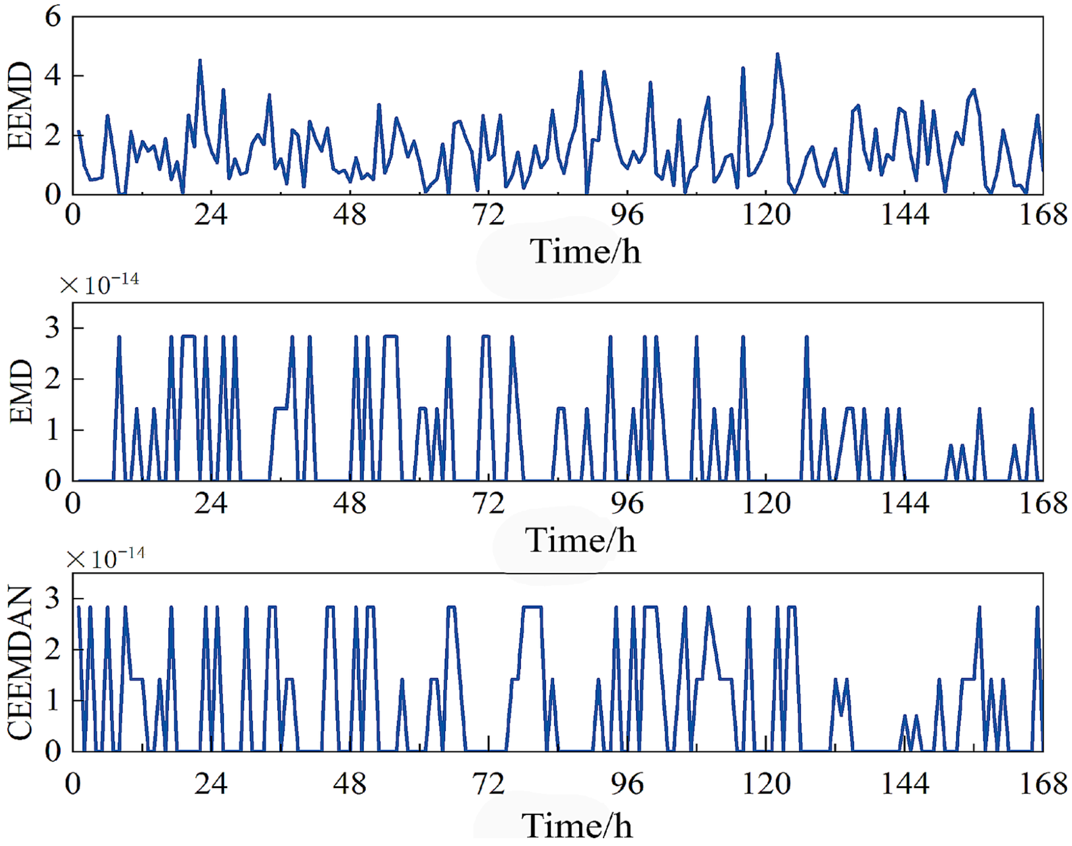

Fig. 15. Comparison of reconstruction errors of different methods.

Table 4
Comparison of test indexes of different methods.

	RE	PCC	SDE	MAPE
EEMD	0.0118	0.9996	1.5639	2.0312
EMD	8.6787×10^{-17}	1	1.2258×10^{-14}	5.4775×10^{-15}
CEEMDAN	8.2334×10^{-17}	1	1.4750×10^{-14}	1.2966×10^{-14}

kW.

The influence of the variation of $P_{el,max,}$ and $P_{fc,max}$ on the system lifetime is shown in Fig. 19. It can be seen that increasing $P_{el,max}$ and $P_{fc,max}$ can push both PEMEL and PEMFC to work more in the high-power operating conditions while reducing the EES operation. Consequently, although both φ_{el} and φ_{fc} increase, φ_{EES} decreases more insignificantly. This causes an overall increase trend in the system degradation rate φ_{HESS}. The system performance degradation rate is low when $P_{el,max}$ is around 60 ∼ 65 kW and $P_{fc,max}$ is around 85 ∼ 100 kW.

The optimized Pareto front and the optimal solution based on NSGA-

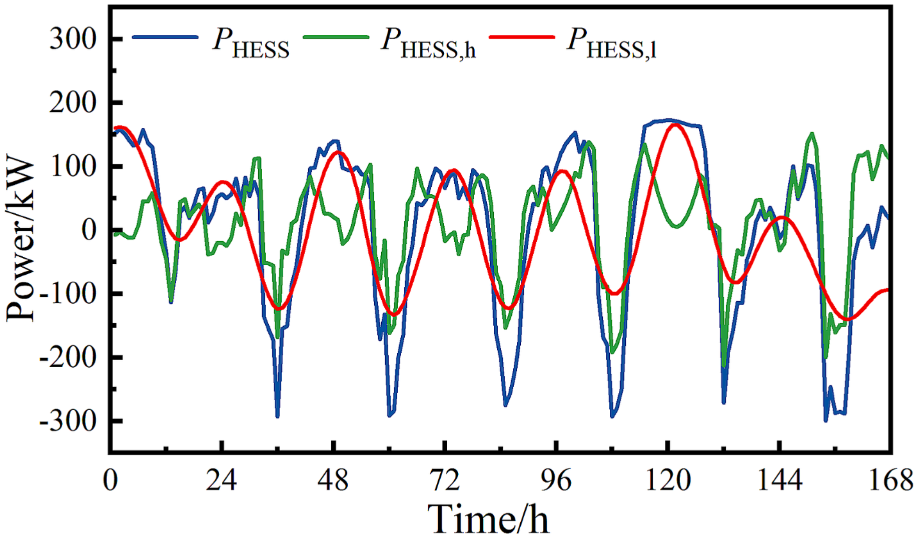

Fig. 16. High-frequency and low-frequency power distribution for TS1.

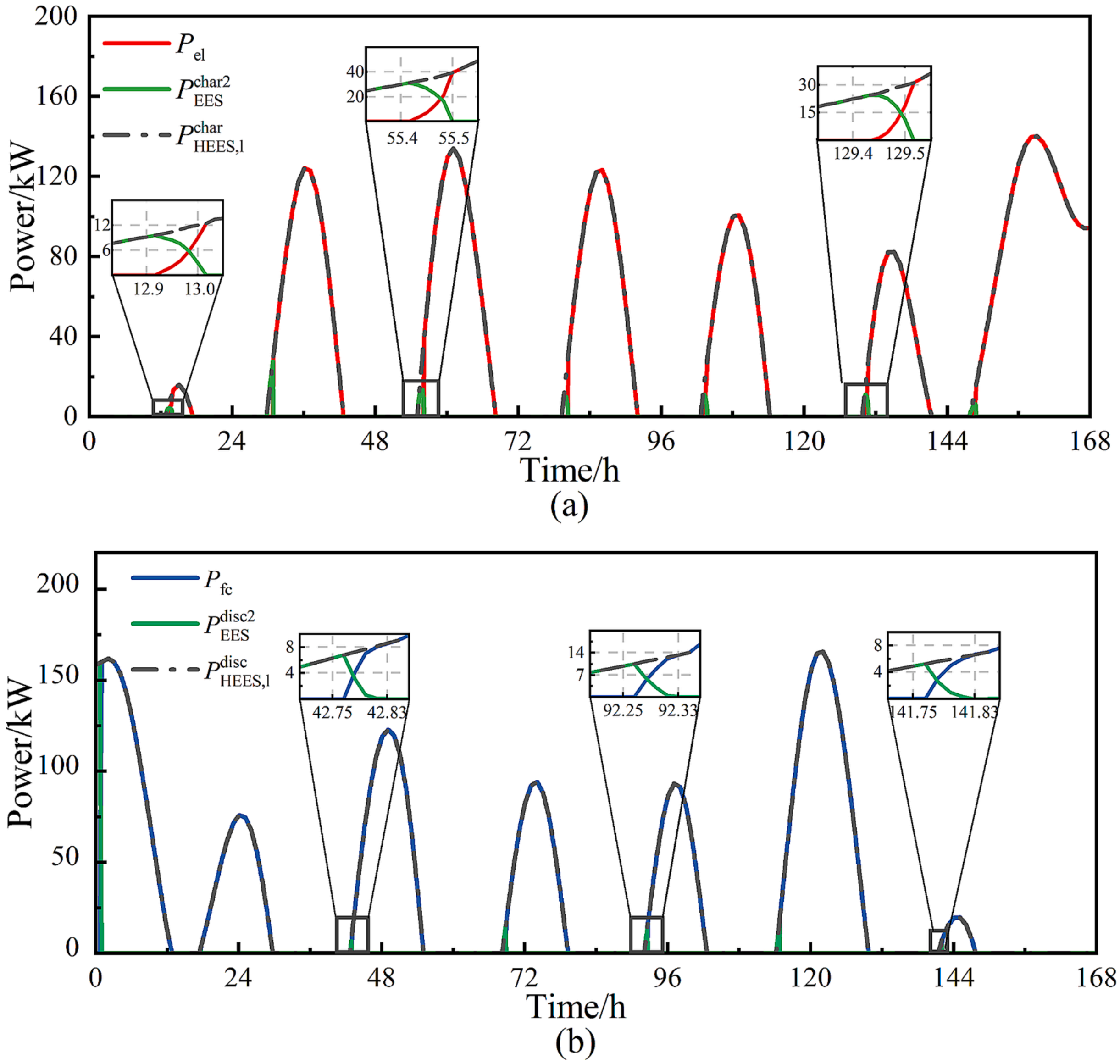

Fig. 17. Operating curve at low-frequency power in (a) charging mode and (b) discharging mode.

III are shown in Fig. 20. It can be seen that the system efficiency F_1 and the system degradation rate F_2 are inversely related, indicating that the system efficiency and the system performance degradation rate are a pair of contradictory indicators. In this work, we select $P_{\mathrm{el,max}} = 97.424$ kW and $P_{\mathrm{fc,max}} = 94.149$ kW as the Pareto optimal solution with $\varphi_{\mathrm{HESS}} = 2.756$ % and $\eta_{\mathrm{sys}} = 69.92$ %. This result is considered to achieve a good balance between durability and efficiency by referring to Fig. 18 and Fig. 19.

5.4. *Synthesis and analysis*

To verify the feasibility of the proposed synergy operation strategy, two conventional schemes are compared:

Scheme I: A single HES system without EES where $P_{\mathrm{el,max}}$ and $P_{\mathrm{fc,max}}$ are optimized using NSGA-III.

Scheme II: A H-E HESS where $P_{\mathrm{el,max}}$ and $P_{\mathrm{fc,max}}$ are not optimized.

The proposed H-E HESS scheme corresponding to that obtained in Section 5.3 is denoted as Scheme III. The power variations of the energy storage devices for the three operation schemes in the four typical scenarios of TS1-TS4 are shown in Fig. 21.

The power variations of PEMEL and PEMFC in Scheme I are shown in Fig. 21(I). In this scheme, the HES system cannot properly handle the power fluctuations due to its delay characteristics during the start-up and also due to the consideration of the system's lifetime. This leads to poor utilization of RES, which in turn causes the unexpected curtailments of wind and solar energy generation. In contrast, from Fig. 21 (II) and (III), it can be seen that only low-frequency power compensation is performed by the HES in the four typical scenarios, and the EES can quickly respond to high-frequency fluctuations and can complement the deficit power of the delayed HES response. Compared to Scheme I, the system efficiency of Scheme II is enhanced by 9.61 %, 12.36 %, 2.34 %, and 4.34 % in TS1 to TS4, respectively, while the efficiency can be further improved in Scheme III by 8.34 %, 4.64 %, 2.34 %, and 2.93 % under the for scenarios. The improvement in Scheme III is attributed to the fact that the energy conversion efficiency of EES is much higher than that of both PEMEL and PEMFC.

The performances of the systems of the three schemes are compared in Table 5. It can be seen that the performance degradation rates of PEMEL and PEMFC in Scheme III are lower than Scheme I in all scenarios. Specifically, the PEMEL and PEMFC degradation rates in TS2 decrease significantly by 1.57 % and 1.09 %, respectively. The degradation of PEMEL and PEMFC is mainly caused by the operations at high

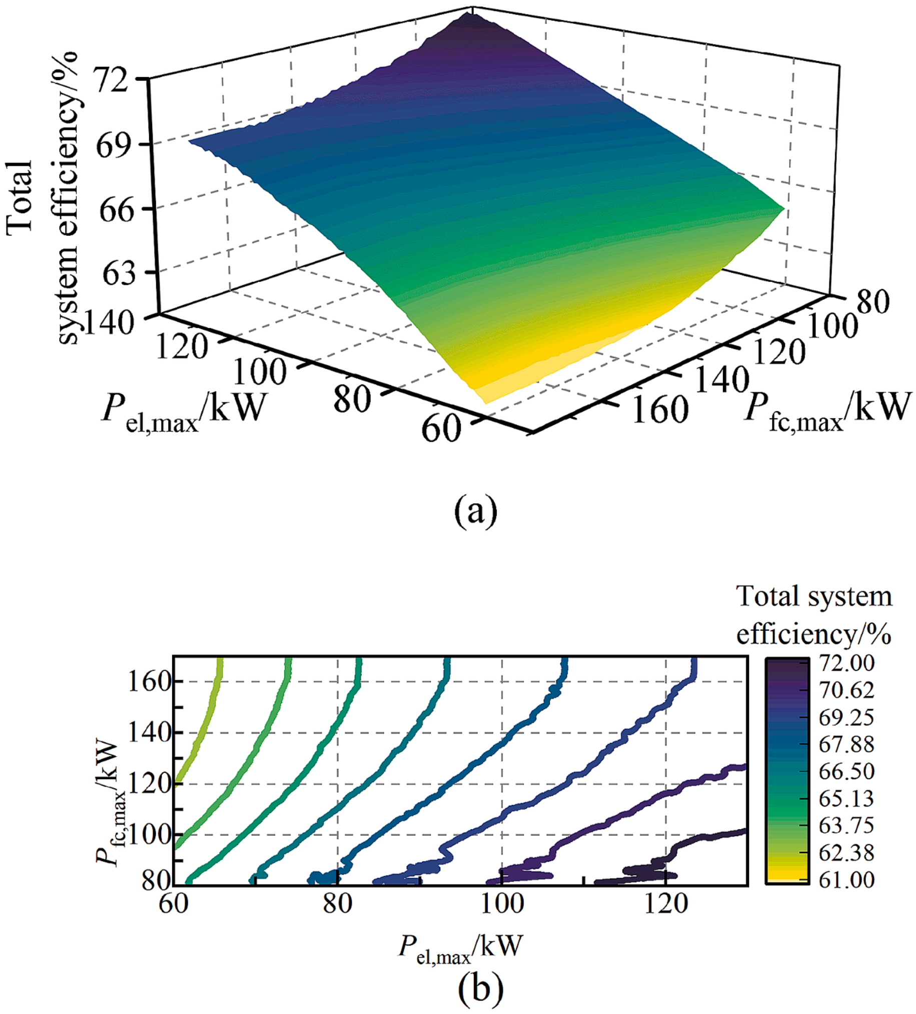

(a)

(b)

Fig. 18. Influence of $P_{\mathrm{el,max}}$ and $P_{\mathrm{fc,max}}$ variation on system efficiency: (a) 3D map; (b) Contour map.

and low power levels, as well as the start-stop operations. The EES can share the high-frequency fluctuation of the system and reduce the start-stop of the HES equipment, which extends HES's lifetime. In addition, the EES system can mitigate the power imbalance between the target and the actual power caused by the response delay of the HES, so the power response speed of the whole system is significantly improved. It is thus verified that the H-E HESS enables higher flexibility compared to the HES alone.

From the comparison of Schemes II and III in Table 5, it can be seen that the optimization management strategy proposed in this study adjusts the target power parameter in the synergy operation strategy with the goal of system efficiency and lifetime, effectively reducing the lifetime degradation rate of H-E HESS. The maximum operating powers of PEMEL and PEMFC in TS1 are reduced by 32.529 kW and 71.614 kW, respectively, and the system performance degradation rate is reduced from 3.47 % to 2.75 %. In addition, compared to Scheme II, the system performance degradation rate of Scheme III is reduced by 0.71 %, 0.54 %, 0.46 %, and 0.21 % in TS1 to TS4. It is shown that the synergy operation strategy optimized using NSGA-III is more effective in the scenario with abundant RES.

Therefore, the synergy operation strategy proposed in this study can effectively improve the response speed to dynamic power demand. The system with the strategy exhibits the highest efficiency and lowest performance degradation rate compared to the other two schemes under comparison.

The power scheduling results in TS1-TS4 based on the proposed algorithm are shown in Fig. 22, where the sampling time is 1 h. It can be seen that in TS1 and TS2, abundant wind and solar resources contribute to high levels of renewable energy generation, whereas the load demand is relatively low. The H-E HESS frequently adjusts its power allocation to satisfy the system demand, leading to significant variations in SOC and LOH. From 120 h to 132 h, both HES and EES in TS1 operate at high power levels. The power demand is solely provided by PEMFC and EES discharges due to the absence of RES. Subsequently, renewable energy generation gradually increases post-132 h, replenishing the energy stores of HST and EES. In TS2, characterized by the richest wind resources, the EES operates most frequently, particularly from 144 h to 168 h, primarily utilizing EES for charging and discharging to balance the power of the system.

From Fig. 22(c) and (d), it can be seen that in TS3 and TS4, the wind and solar resources are scarce, the renewable energy generation is low, and the load power demand is relatively large. Therefore, to prevent large-scale load shedding and power outages, PEMFC and EES operate more frequently, resulting in a significant decrease in SOC and LOH levels after the 168-hour operation, but they remain within the specified limits. In TS3, the output of renewable PV is relatively limited. There is a substantial shortage of renewable energy during the periods 72–108 h and 132–156 h, in which case the PEMFC and EES work together to provide the load demand power. In TS4, PV output is the least. Load demand power is mainly supported by WT and additional storage systems, which produce power to supply load demand mainly during 24–48 h, 72–84 h, and 120–168 h.

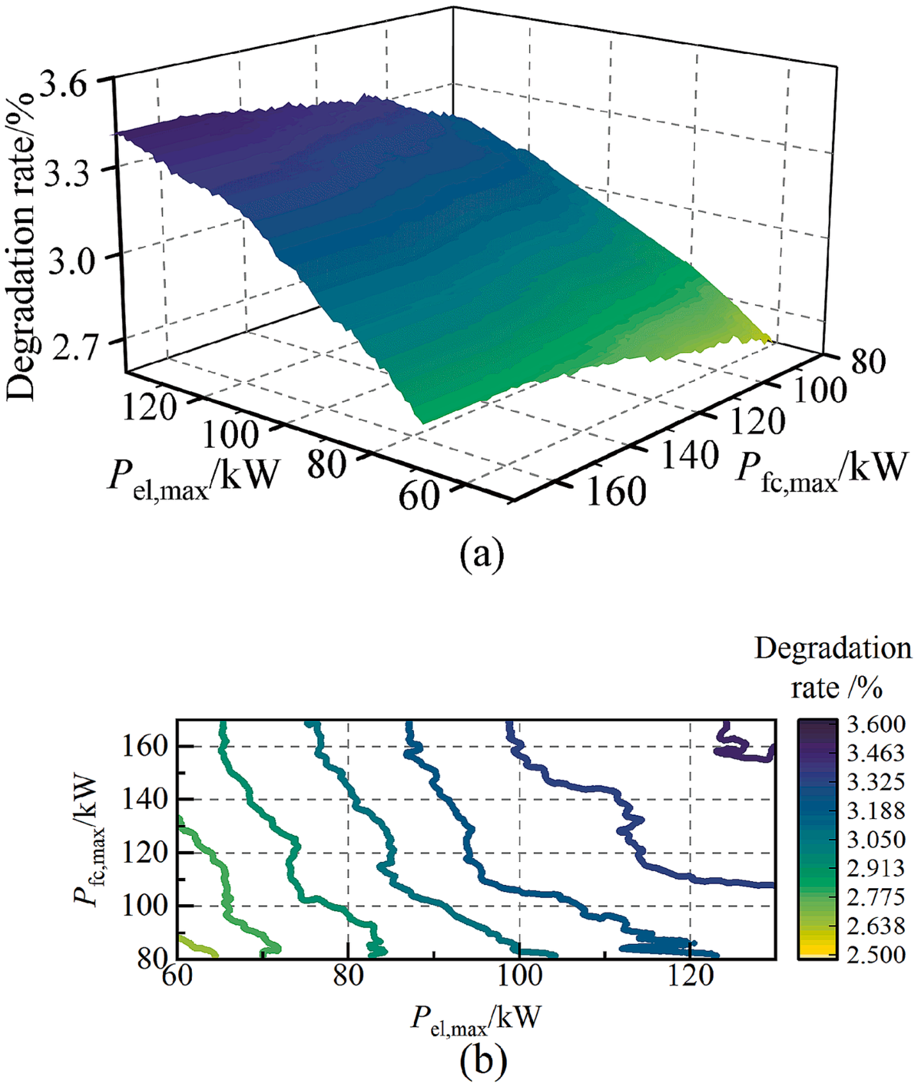

Fig. 19. Influence of $P_{el,max}$ and $P_{fc,max}$ variation on degradation rate: (a) 3D map; (b) Contour map.

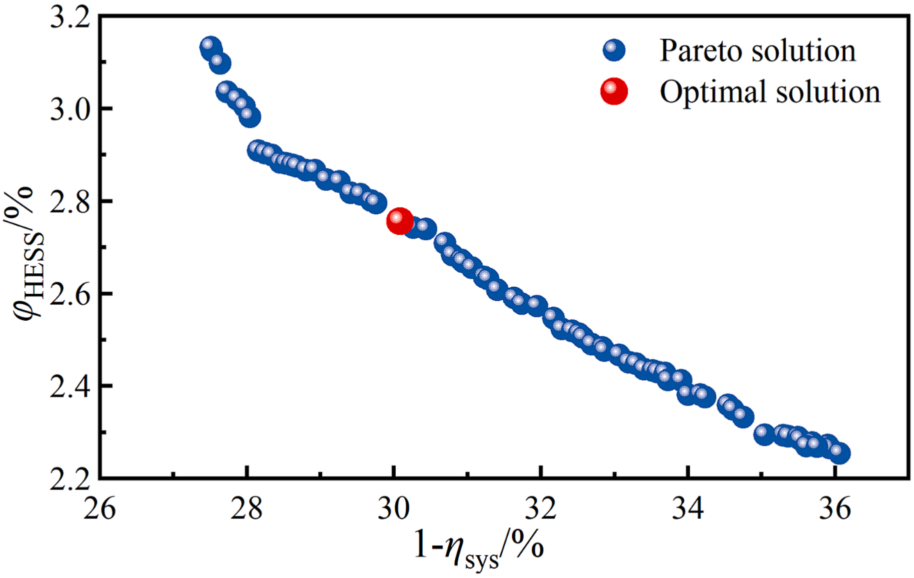

Fig. 20. Pareto front and optimal solution of NSGA-III.

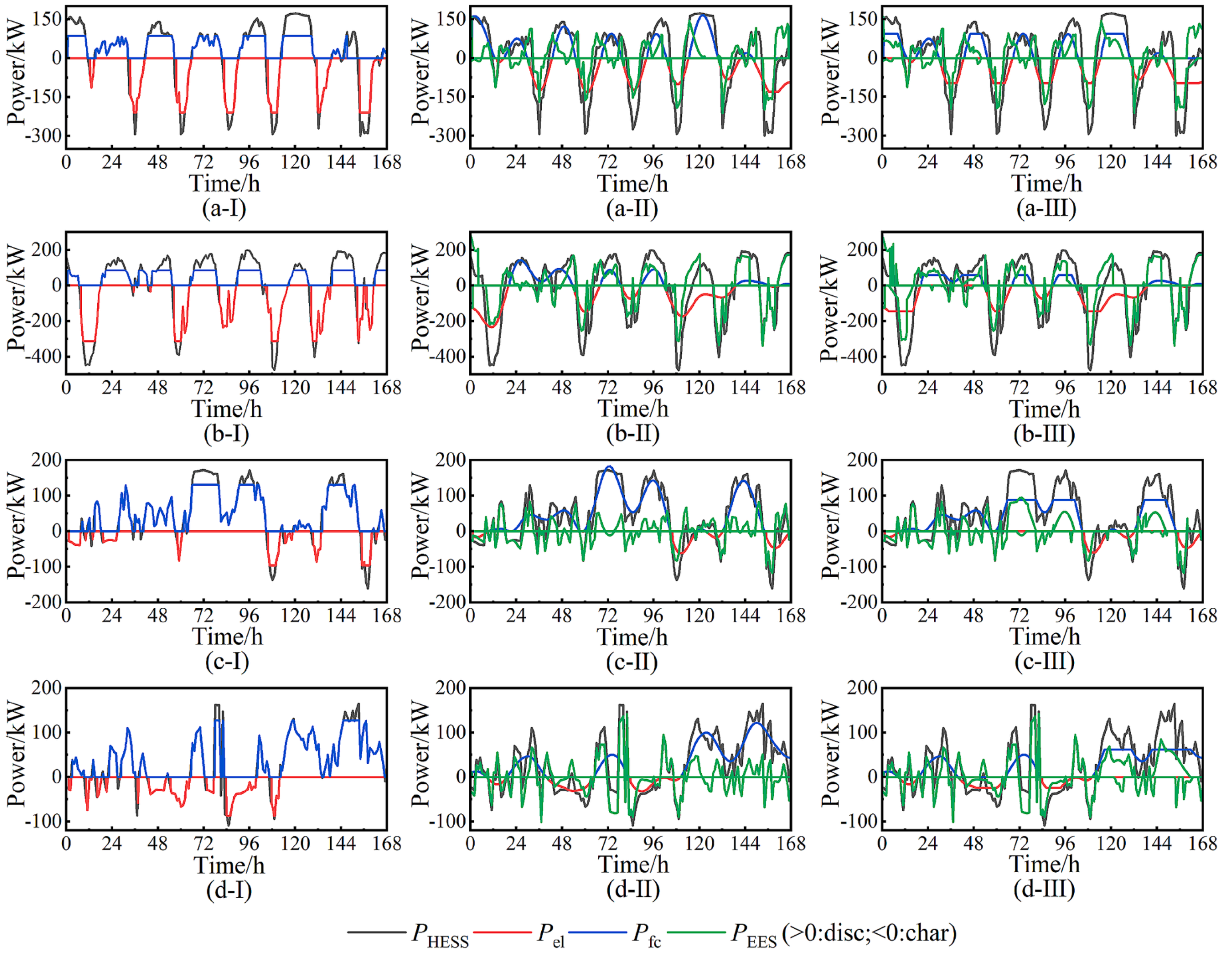

Fig. 21. Comparison of power profiles of three schemes under (a) TS1, (b) TS2, (c) TS3, and (d) TS4.

Table 5
Performance comparison of three schemes under TS1-TS4.

Scenario	Scheme	$P_{\mathrm{el,max}}$/kW	$P_{\mathrm{fc,max}}$/kW	φ_{el}/%	φ_{fc}/%	φ_{EES}/%	φ_{HESS}/%	η_{sys}/%	Response Time
TS1	Scheme I	209.28	86.26	2.22	1.54	/	3.76	51.97	0.5 h
	Scheme II	129.95	165.76	1.85	1.31	0.31	3.47	61.58	<1 s
	Scheme III	97.42	94.15	1.23	1.09	0.45	2.76	69.92	<1 s
TS2	Scheme I	314.34	85.01	3.62	1.73	/	5.35	51.17	0.5 h
	Scheme II	233.86	142.98	2.34	0.89	0.65	3.87	63.53	<1 s
	Scheme III	143.52	60.09	2.05	0.64	0.64	3.33	68.17	<1 s
TS3	Scheme I	95.67	131.10	0.39	1.94	/	2.32	56.97	0.5 h
	Scheme II	62.22	182.68	0.12	1.53	0.22	1.88	59.48	<1 s
	Scheme III	58.95	88.13	0.07	1.12	0.23	1.42	61.82	<1 s
TS4	Scheme I	87.49	127.23	0.23	1.45	/	1.68	56.54	0.5 h
	Scheme II	32.10	182.68	0.09	0.91	0.18	1.18	60.88	<1 s
	Scheme III	24.21	69.29	0.09	0.65	0.23	0.97	63.81	<1 s

The strategy proposed in this study was also tested in a H-E HESS-integrated DC microgrid demonstration project shown in Fig. 8. A power analyzer was used to record the power generated by the PEMFC and the power supplied to the PEMEL, and discharge tests measured the total power and SOC of the EES system. The mass of hydrogen stored in each tank was obtained by volumetric mass conversion and accumulated to obtain the system LOH. The measured power situation and energy reserve variation data for each energy storage device are shown in Fig. 23.

From Fig. 23, it can be seen that under the test results, each energy

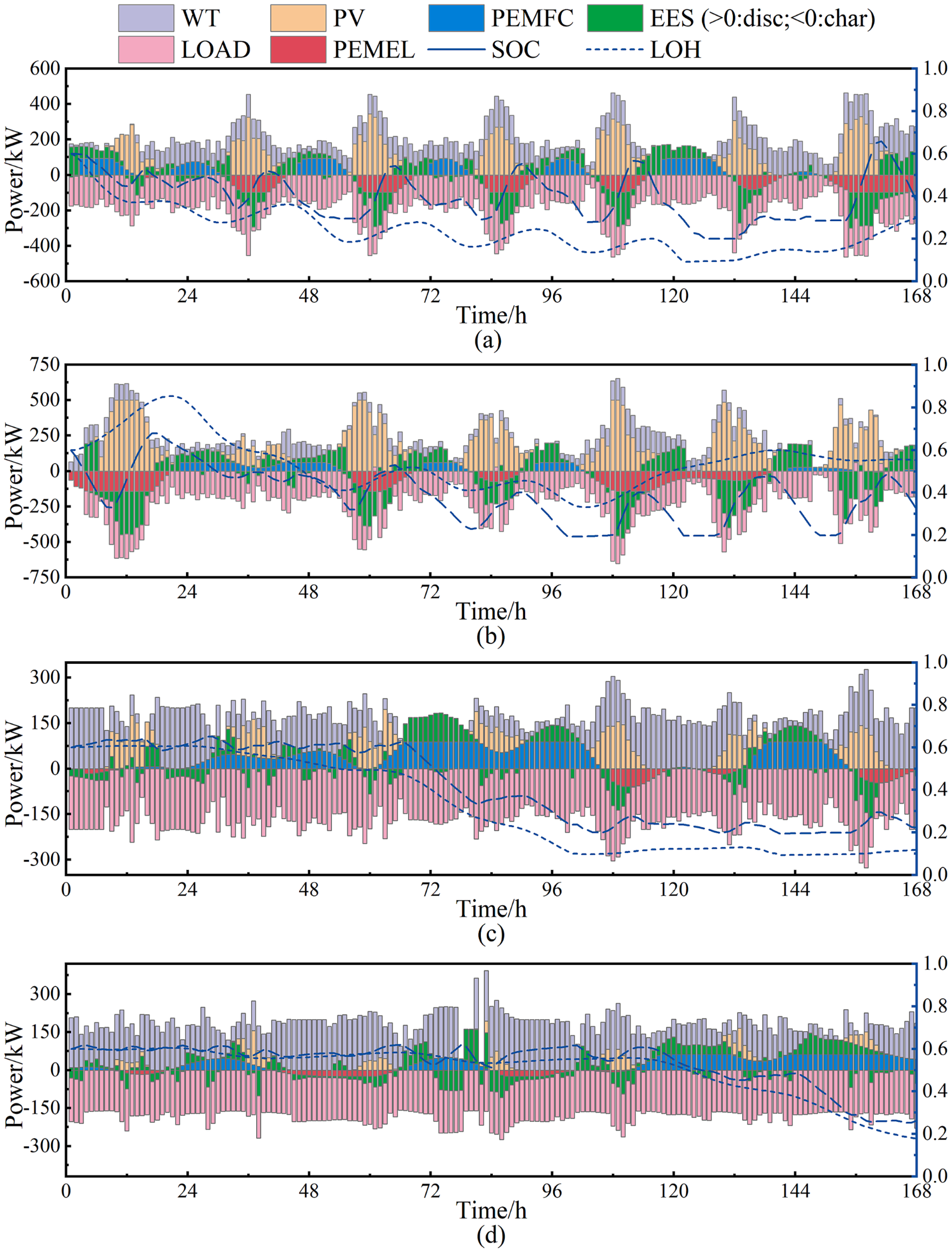

Fig. 22. Power flow in (a) TS1, (b) TS2, (c) TS3, (d) and TS4.

storage device can operate normally according to the synergy operation strategy. The EES system handles the high-frequency power, the HES system handles the low-frequency power, and the PEMEL and PEMFC are operated at their maximum power levels. The operating power of each energy storage device is aligned with the proposed strategy, and the SOC and LOH levels are well-controlled within the allowable ranges. In summary, both the simulation results tested under the four typical scenarios and the experimental results in the demonstration project verify that the system can achieve the expected high performance. The energy management system can coordinate and control the microgrid to

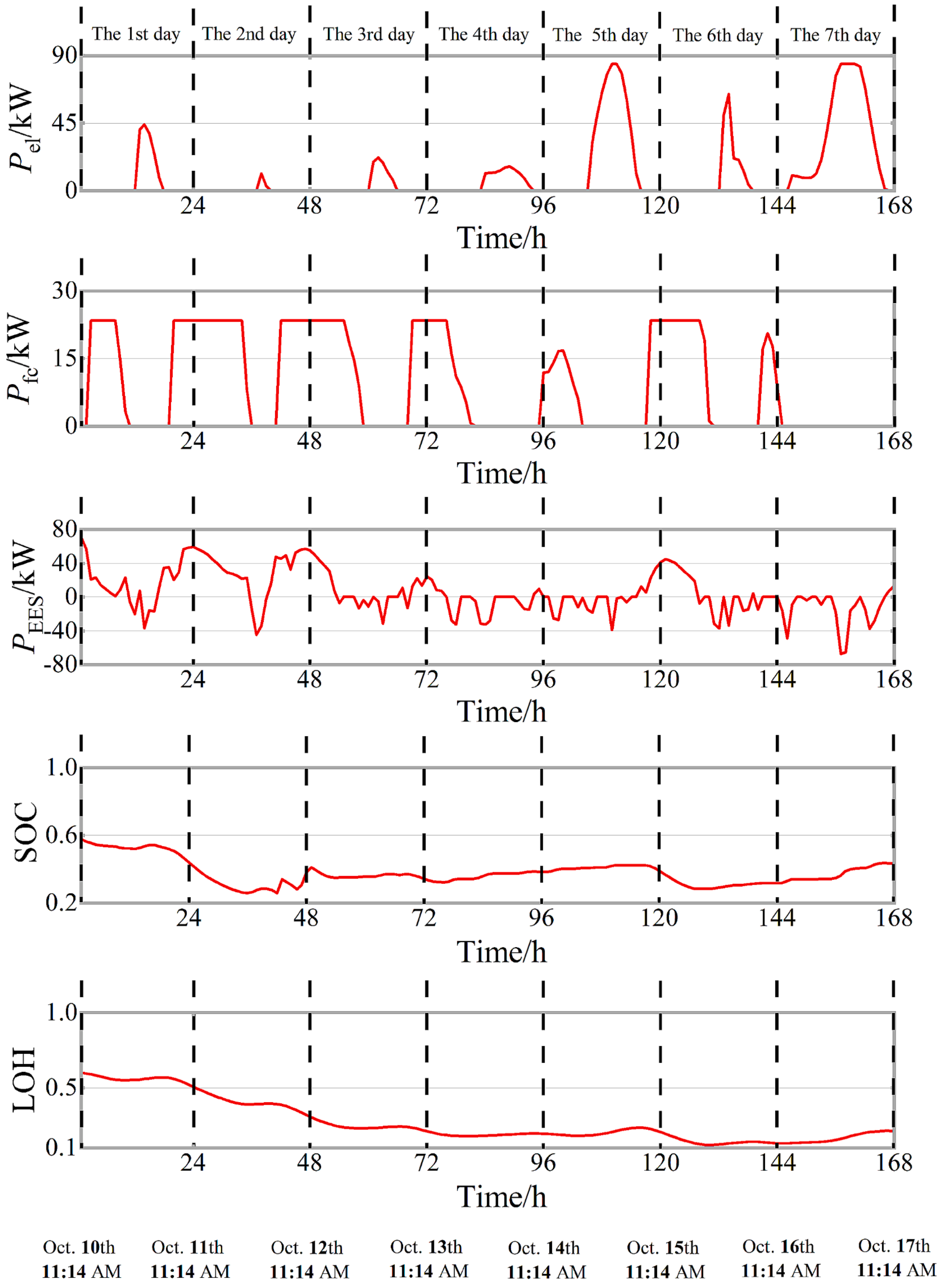

Fig. 23. Power profiles and energy reserve changes for each energy storage device.

maintain the balance of power and electricity to meet the normal power demand of internal loads. This further verifies the feasibility of the synergy operation strategy proposed in this study.

6. Conclusion

In this study, to coordinate the complementary operation of HES and EES, we consider the effects of power, response time, lifetime, and efficiency, carry out the power-matching design, and propose a synergy operation strategy for H-E HESS that take into account the lifetime and response characteristics. CEEMDAN-HT was used to reconstruct the H-E HESS power into high-frequency components and low-frequency components to allocate the power for EES and HES and develop a synergy operation strategy based response on delay characteristics during hydrogen storage start-up. Finally, the NSGA-III algorithm is used to optimize the target power parameters in the synergy operation strategy. The conclusions of this paper are as follows:

1) To address the problem of the adaptability of hydrogen and electric energy storage at different scales of high and low frequencies, the

CEEMDAN-HT method realizes the minimization of the high-frequency fluctuation component of the mixing in HES and the low-frequency fluctuation component of the mixing in EES, so that the mixing energy can be reduced to 0.139. This method efficiently mitigates the negative impacts of the rapid power changes on the key components of the HES system.

2) To address the response delay characteristic of the HES system, a synergy operation strategy is proposed to utilize electric energy storage to supplement the power difference in the hydrogen energy storage system during the start-up phase. It reduces the system energy waste and improves the dynamic characteristics of the system, reducing the system response time from 0.5 h to less than 1 s.
3) Multiobjective optimization of key parameters of the energy management strategy using the NSGA-III algorithm further improves the lifetime and efficiency of the H-E HESS. The optimized system efficiency can reach 69.92 % with a system performance degradation rate of 2.76 % if the operation scenario is adequately selected. Compared with the unoptimized strategy, the system efficiency increased by 8.34 %, and the performance degradation rate decreased by 0.71 %. Compared with the operation of a single hydrogen energy storage system, the system efficiency increased by 17.95 %, and the performance degradation rate decreased by 1 %. The results of the demonstration project test verified the efficacy of the proposed synergy operation strategy.

However, this study has certain limitations. The analysis conducted provides direction for the optimization of system point power operation, but detailed optimization of the internal system remains a field requiring further research. Additionally, the thermal factors in PEMEL and PEMFC are crucial in engineering projects but have not been fully incorporated into this study. Future research will delve into the multi-energy flow thermoelectric operation of the system, enhancing the breadth and depth of understanding in this area. Furthermore, we will explore how operating parameters such as temperature and pressure affect storage system lifespan, incorporating advanced modeling techniques and experimental validation to quantify their impact. This will be complemented by the potential inclusion of adaptive control mechanisms to dynamically optimize system performance under varying operating conditions, thereby improving both efficiency and longevity.

CRediT authorship contribution statement

Banghua Du: Writing – original draft, Methodology. **Yanyu Peng:** Software, Data curation. **Yang Li:** Validation, Supervision. **Changjun Xie:** Writing – review & editing, Project administration, Funding acquisition. **Shihao Zhu:** Visualization, Data curation. **Wenchao Zhu:** Formal analysis. **Yang Yang:** Conceptualization. **Li You:** Funding acquisition. **Leiqi Zhang:** Investigation. **Bo Zhao:** Project administration.

Declaration of competing interest

The authors declare the following financial interests/personal relationships which may be considered as potential competing interests: Xie Changjun reports financial support was provided by National Key Research and Development Program of China. Reports a relationship with that includes:. Has patent pending to. If there are other authors, they declare that they have no known competing financial interests or personal relationships that could have appeared to influence the work reported in this paper.

Acknowledgment

This paper is supported by the National Key Research and Development Program of China (No. 2020YFB1506802).

Data availability

Data will be made available on request.

References

[1] Capurso T, Stefanizzi M, Torresi M, Camporeale SM. Perspective of the role of hydrogen in the 21st century energy transition. Energ Conver Manage 2022;251:114898.
[2] Zhao H, Xu J, Xu K, Sun J, Wang Y. Optimal allocation method of source and storage capacity of PV-hydrogen zero carbon emission microgrid considering the usage cost of energy storage equipment. Energies 2022;15(13):4916.
[3] Nikolaidis P, Poullikkas A. Cost metrics of electrical energy storage technologies in potential power system operations. Sustain Energy Technol Assess 2018;25:43–59.
[4] Vichos E, Sifakis N, Tsoutsos T. Challenges of integrating hydrogen energy storage systems into nearly zero-energy ports. Energy 2022;241:122878.
[5] Yang Y, De La Torre B, Stewart K, Lair L, Phan NL, Das R, et al. The scheduling of alkaline water electrolysis for hydrogen production using hybrid energy sources. Energ Conver Manage 2022;257:115408.
[6] Henao N, Kelouwani S, Agbossou K, Dubé Y. Proton exchange membrane fuel cells cold startup global strategy for fuel cell plug-in hybrid electric vehicle. J Power Sources 2012;220:31–41.
[7] Varela C, Mostafa M, Zondervan E. Modeling alkaline water electrolysis for power-to-x applications: a scheduling approach. Int J Hydrogen Energy 2021;46(14):9303–13.
[8] Chen Q, Kuang Z, Liu X, Zhang T. Energy storage to solve the diurnal, weekly, and seasonal mismatch and achieve zero-carbon electricity consumption in buildings. Appl Energy 2022;312:118744.
[9] Yamashita D, Tsuno K, Koike K, Fujii K, Wada S, Sugiyama M. Distributed control of a user-on-demand renewable-energy power-source system using battery and hydrogen hybrid energy-storage devices. Int J Hydrogen Energy 2019;44(50):27542–52.
[10] Feng Q, Liu G, Wei B, Zhang Z, Li H, Wang H. A review of proton exchange membrane water electrolysis on degradation mechanisms and mitigation strategies. J Power Sources 2017;366:33–55.
[11] Zhao J, Li X. A review of polymer electrolyte membrane fuel cell durability for vehicular applications: degradation modes and experimental techniques. Energ Conver Manage 2019;199:112022.
[12] Hannan MA, Abu SM, Al-Shetwi AQ, Mansor M, Ansari MNM, Muttaqi KM, et al. Hydrogen energy storage integrated battery and supercapacitor based hybrid power system: a statistical analysis towards future research directions. Int J Hydrogen Energy 2022;47(93):39523–48.
[13] Hettiarachchi D, Rajakaruna S, Ghosh A. A new approach to identify the optimum frequency ranges of the constituent storage devices of a hybrid energy storage system using the empirical mode decomposition technique. J Storage Mater 2022;51:104285.
[14] Yan Y, Wang X, Ren F, Shao Z, Tian C. Wind speed prediction using a hybrid model of EEMD and LSTM considering seasonal features. Energy Rep 2022;8:8965–80.
[15] Jiang Y, Zheng L, Ding X. Ultra-short-term prediction of photovoltaic output based on an LSTM-ARMA combined model driven by EEMD. J Renew Sustain Energy 2021;13(4).
[16] Feng ZK, Niu WJ, Wan XY, Xu B, Zhu FL, Chen J. Hydrological time series forecasting via signal decomposition and twin support vector machine using cooperation search algorithm for parameter identification. J Hydrol 2022;612:128213.
[17] Wang Y, Yuan Z, Liu H, Xing Z, Ji Y, Li H, et al. A new scheme for probabilistic forecasting with an ensemble model based on CEEMDAN and AM-MCMC and its application in precipitation forecasting. Expert Syst Appl 2022;187:115872.
[18] Du B, Zhu S, Zhu W, Lu X, Li Y, Xie C, et al. Energy management and performance analysis of an off-grid integrated hydrogen energy utilization system. Energ Conver Manage 2024;299:117871.
[19] Fan G, Liu Z, Liu X, Shi Y, Wu D, Guo J, et al. Energy management strategies and multiobjective optimization of a near-zero energy community energy supply system combined with hybrid energy storage. Sustain Cities Soc 2022;83:103970.
[20] Kamel AA, Rezk H, Abdelkareem MA. Enhancing the operation of fuel cell-photovoltaic-battery-supercapacitor renewable system through a hybrid energy management strategy. Int J Hydrogen Energy 2021;46(8):6061–75.
[21] Han Y, Zhang G, Li Q, You Z, Chen W, Liu H. Hierarchical energy management for PV/hydrogen/battery island DC microgrid. Int J Hydrogen Energy 2019;44(11):5507–16.
[22] Rezk H, Nassef AM, Abdelkareem MA, Alami AH, Fathy A. Comparison among various energy management strategies for reducing hydrogen consumption in a hybrid fuel cell/supercapacitor/battery system. Int J Hydrogen Energy 2021;46(8):6110–26.
[23] Ferrario AM, Bartolini A, Manzano FS, Vivas FJ, Comodi G, McPhail SJ, et al. A model-based parametric and optimal sizing of a battery/hydrogen storage of a real hybrid microgrid supplying a residential load: Towards island operation. Adv Appl Energy 2021;3:100048.
[24] Li B, Miao H, Li J. Multiple hydrogen-based hybrid storage systems operation for microgrids: a combined TOPSIS and model predictive control methodology. Appl Energy 2021;283:116303.
[25] Adeyemo AA, Amusan OT. Modelling and multi-objective optimization of hybrid energy storage solution for photovoltaic powered off-grid net zero energy building. J Storage Mater 2022;55:105273.

[26] Pu Y, Li Q, Zou X, Li R, Li L, Chen W, et al. Optimal sizing for an integrated energy system considering degradation and seasonal hydrogen storage. Appl Energy 2021;302:117542.

[27] Yousri D, Farag HE, Zeineldin H, El-Saadany EF. Integrated model for optimal energy management and demand response of microgrids considering hybrid hydrogen-battery storage systems. Energ Conver Manage 2023;280:116809.

[28] Li B, Roche R, Paire D, Miraoui A. Sizing of a stand-alone microgrid considering electric power, cooling/heating, hydrogen loads and hydrogen storage degradation. Appl Energy 2017;205:1244–59.

[29] Zhang Y, Hua QS, Sun L, Liu Q. Life cycle optimization of renewable energy systems configuration with hybrid battery/hydrogen storage: a comparative study. J Storage Mater 2020;30:101470.

[30] Liu Z, Li Y, Fan G, Wu D, Guo J, Jin G, et al. Co-optimization of a novel distributed energy system integrated with hybrid energy storage in different nearly zero energy community scenarios. Energy 2022;247:123553.

[31] Khatib FN, Wilberforce T, Ijaodola O, Ogungbemi E, El-Hassan Z, Durrant A, et al. Material degradation of components in polymer electrolyte membrane (PEM) electrolytic cell and mitigation mechanisms: a review. Renew Sustain Energy Rev 2019;111:1–14.

[32] Guilbert D, N'Diaye A, Luberda P, Djerdir A. Fuel cell lifespan optimization by developing a power switch fault-tolerant control in a floating interleaved boost converter. Fuel Cells 2017;17(2):196–209.

[33] Boudraa AO, Cexus JC. EMD-based signal filtering. IEEE Trans Instrum Meas 2007;56(6):2196–202.

[34] Deng M, Deng A, Zhu J, Sun W. Adaptive bandwidth Fourier decomposition method for multi-component signal processing. IEEE Access 2019;7:109776–91.

[35] Yan J, Hu L, Zhen Z, Wang F, Qiu G, Li Y, et al. Frequency-domain decomposition and deep learning based solar PV power ultra-short-term forecasting model. IEEE Trans Ind Appl 2021;57(4):3282–95.

[36] Hu K, Chu T, Li F, Wang B, Zhang Z, Liu T. Effect of different control strategies on rapid cold start-up of a 30-cell proton exchange membrane fuel cell stack. Int J Hydrogen Energy 2021;46(62):31788–97.

[37] Buttler A, Spliethoff H. Current status of water electrolysis for energy storage, grid balancing and sector coupling via power-to-gas and power-to-liquids: a review. Renew Sustain Energy Rev 2018;82:2440–54.

[38] Zhang Z, Miyajima R, Inada T, Miyagi D, Tsuda M. Novel energy management method for suppressing fuel cell degradation in hydrogen and electric hybrid energy storage systems compensating renewable energy fluctuations. Int J Hydrogen Energy 2018;43(14):6879–86.

[39] Wang Q, Yang P, Buja G. Design and analysis on different functions of battery energy storage system for thermal power units frequency regulation. Energy Rep 2022;8:11981–91.

[40] Herrera VI, et al. Optimal energy management and sizing of a battery–supercapacitor-based light rail vehicle with a multiobjective approach. IEEE Trans Ind Appl 2016;52(4):3367–77.

[41] Lu X, Du B, Zhou S, Zhu W, Li Y, Yang Y, et al. Optimization of power allocation for wind-hydrogen system multi-stack PEM water electrolyzer considering degradation conditions. Int J Hydrogen Energy 2023;48(15):5850–72.

[42] Jahromi MM, Heidary H. Durability and economics investigations on triple stack configuration and its power management strategy for fuel cell vehicles. Int J Hydrogen Energy 2021;46(7):5740–55.

[43] Olabi AG, Wilberforce T, Abdelkareem MA. Fuel cell application in the automotive industry and future perspective. Energy 2021;214:118955.

[44] Scheepers F, Stähler M, Stähler A, Rauls E, Müller M, Carmo M, et al. Improving the efficiency of PEM electrolyzers through membrane-specific pressure optimization. Energies 2020;13(3):612.

[45] García-Triviño P, Fernández-Ramírez LM, Gil-Mena AJ, Llorens-Iborra F, García-Vázquez CA, Jurado F. Optimized operation combining costs, efficiency and lifetime of a hybrid renewable energy system with energy storage by battery and hydrogen in grid-connected applications. Int J Hydrogen Energy 2016;41(48):23132–44.

[46] Cheng YY, Chai ZY, Li YL. Many-objective many-task optimization using reference-points-based nondominated sorting approach. Futur Gener Comput Syst 2023;145:496–510.

[47] Xue F, Wu D. NSGA-III algorithm with maximum ranking strategy for many-objective optimisation. Int J Bio-Inspired Comput 2020;15(1):14–23.

[48] Abdi Y, Feizi-Derakhshi MR. Hybrid multi-objective evolutionary algorithm based on search manager framework for big data optimization problems. Appl Soft Comput 2020;87:105991.

[49] Khettabi I, Boutiche MA, Benyoucef L. NSGA-II vs NSGA-III for the sustainable multi-objective process plan generation in a reconfigurable manufacturing environment. IFAC-PapersOnLine 2021;54(1):683–8.

[50] Liu Y, You K, Jiang Y, Wu Z, Liu Z, Peng G, et al. Multi-objective optimal scheduling of automated construction equipment using non-dominated sorting genetic algorithm (NSGA-III). Autom Constr 2022;143:104587.